Design and Evaluation of a 300 kW Double Stage Axial-Flux Permanent Magnet Generator

by

David Natangue Mbidi

Thesis presented in partial fulfilment of the requirements for the degree of Maters of Science in Electrical Engineering at the University of Stellenbosch

Supervisor: Prof. M. J. Kamper

December 2001

Stellenbosch University http://scholar.sun.ac.za

DECLARATION

I, the undersigned, hereby declare that the work contained in this thesis is my own original work and that I have not previously in its entirety or in part submitted it at any University for a degree.

Signature: Date:

Place:

Stellenbosch University http://scholar.sun.ac.za

ABSTRACT

This thesis deals with the design and evaluation of a 300 kW double stage axial-flux permanent magnet generator with an ironless stator. The magnetic and electrical design equations are derived for sinewave and quasi-squarewave axial-flux permanent magnet machines. The thermal design approach used is also described. The machine is optimised for maximum torque per current loading. A Matlab program code is developed to do the necessary calculations in the design optimisation and the calculation of the machine parameters.

Mechanical finite element simulations are conducted to investigate the severity of the magnetic attraction force between the rotor discs. The results obtained from the simulations suggested an increase in the yoke thickness in order to withstand the attraction force. The construction of the prototype machine's rotor and stator is described. The flux density in the airgap is thoroughly investigated through measurements and analysis. Thermal measurements are also conducted to investigate the effect of eddy currents in the stator winding. Furthermore, no-load measurements conducted on the 300 kW machine showed that the machine has a serious problem of circulating currents in the parallel connected coils. Possible solutions for this are investigated and recommendations are given. Due to the circulating current problem and the relative high eddy current losses, it was not possible to do full-load tests on the machine.

Stellenbosch University http://scholar.sun.ac.za

OPSOMMING

Hierdie tesis handel oor die ontwerp en evaluering van 'n multi-stadium Aksiale Vloed Permanente Magneet (AFPM) masjien met 'n ysterlose stator. Die magnetiese - en elektriese ontwerp-vergelykings is afgelei vir sinusgolf en quasi vierkantsgolf AFPM masjiene. Die termiese ontwerp word ook bespreek. Die masjien is geoptimeer vir maksimum draaimoment per stroombelasting. Daar is 'n program-kode in Matlab geskryf om die nodige berekeninge vir die optimering van die masjien uit te voer en vir die bepaling van die masjien-parameters.

Meganiese eindige element berekenings is gedoen om die invloed van die magnetiese aantrekkingskrag tussen die rotorskywe te ondersoek. Die resultate het aangedui dat die rotorskyfdikte nie die magnetiese aantrekkingskrag van die magnete kan weerstaan nie en moes in dikte vedubbel word. Die konstruksie van die masjien se rotor en stator is behandel. Die vloeddigtheid in die luggaping is noukeurig ondersoek deur metings en analise. Termiese metings is ook gedoen om die invloed van die werwel strome in die statorwikkelings te ondersoek. Verder het die nullas-toetse wat gedoen is op die masjien, aangedui dat die masjien 'n ernstige probleem het met sirkulerende strome in die parallelle geleiers van die statorspoele. Moontlike oplossings is ondersoek en aanbevelings word gegee. Dit was nie moontlik om vollastoetse op die masjien te doen nie, as gevolg van die probleem met sirkulerende strome en die relatief hoë werwelstoom-verliese in die statorwikkelings.

Stellenbosch University http://scholar.sun.ac.za

ACKNOWLEDGEMENTS

I first of all would like to give praise to God for giving me strength and salvation.

I would also like to thank my supervisor, Prof. M. J. Kamper, for his guidance and advice through the course of the project.

The following persons are acknowledged for their invaluable contributions to the project and I would, thus, like to extend my sincere appreciation to them:

- J. Blom, K. van der Westhuizen and J. Weerdenburg for their contributions in the mechanically related aspects.
- All my colleagues and the electrical workshop staff.
- My family and friends for encouragement and support.
- PETROFUND and the Electrical Machines Group for financial support.

Stellenbosch University http://scholar.sun.ac.za

CONTENTS

Stellenbosch University http://scholar.sun.ac.za

Stellenbosch University http://scholar.sun.ac.za

LIST OF TABELS

Stellenbosch University http://scholar.sun.ac.za

LIST OF FIGURES

Stellenbosch University http://scholar.sun.ac.za

Stellenbosch University http://scholar.sun.ac.za

Stellenbosch University http://scholar.sun.ac.za

GLOSSARY OF ABBREVIATIONS

AFPM	Axial-Flux Permanent Magnet
AFM	Axial-Flux Machine
AFPMG	AFPM generator
RFM	Radial Flux Machine
BDC	Brushless DC
EMF	Electromotive Force
FEA	Finite Element Analysis
FE	Finite Element
FEM	Finite Element Method
LCM	Lumped Circuit Method
MMF	Magnetomotive Force
NdFeB	Neodymium-Iron-Boron
PM	Permanent Magnet

Stellenbosch University http://scholar.sun.ac.za

LIST OF SYMBOLS

j	number of stages
r_o	machine outer radius [m]
r_i	machine inner radius [m]
r_{avg}	machine average radius [m]
Δl	stator active length [m]
l_g	airgap length [m]
t_{cu}	active stator winding thickness [m]
t_y	yoke thickness [m]
y_h	yoke thickness [m]
l_{ipg}	inter polar gap [m]
l_e	total end winding length [m]
l_{e1}-l_{e3}	end winding length sections [m]
l_m	magnet thickness [m]
A_m	magnet area [m^2]
A_{ag}	airgap area [m^2]
A_{coil}	coil area [m^2]
A_{con}	conductor area [m^2]
p	number of poles
B_m	magnet flux density [T]
B_g	airgap flux density [T]
B_r	magnet remanence flux density [T]
φ_r	magnet remanence flux [Wb]
φ_{ag}	airgap flux [Wb]
R_{ag}	airgap reluctance [A/Wb]
R_c	yoke reluctance [A/Wb]
R_m	magnet reluctance [A/Wb]
μ_{rec}	relative recoil permeability [H/m]
θ_{ip}	inter polar angle [rad]
θ_{se}	coil span in electrical degrees [rad]

Stellenbosch University http://scholar.sun.ac.za

J	current density [A/m^2]
m	number of phases
a	number of parallel coils
q	number of coils per pole per phase
k_f	filling factor
I_s	feeding current [A]
I_{ph}	phase current [A]
N_c	number of turns per coil
N_{ph}	number of turns in series per phase
R_{ph}	phase resistance [Ω]
k	ratio of magnet angle over pole pitch
n	angular speed [rev/s]
n_{cp}	number of phase coil conductors in parallel
D_{wire}	diameter of phase coil conductor

ρ_m	magnet mass density [kg/m^2]
ρ_y	yoke mass density [kg/m^2]
ρ_{cu}	copper mass density [kg/m^2]
V_y	active volume of yoke [m^3]
V_{cu}	active copper volume [m^3]
V_m	volume of magnets [m^3]
S_{tg}	number of machine stages
$Mass_y$	mass of machine yoke
$Mass_w$	mass of stator winding
$Mass_m$	mass of magnets

Stellenbosch University http://scholar.sun.ac.za

1. INTRODUCTION

Historically, the earliest electrical machines were axial-flux machines (AFMs). Faraday invented a primitive disc dynamo in 1831, which was in the form of an AFM shown schematically in Figure 1.1 [1]. Later in that year, Pixii's machine followed which is shown diagrammatically in Figure 1.2. This machine had all the essential elements of the modern machine such as

- the field-generating magnets, rather than field windings on the rotor,
- the output was AC rather then DC voltage and current,
- the airgap could be made quite large,
- and the system could be made multi-polar.

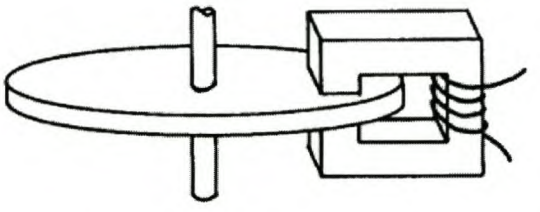

Figure 1.1: Schematic arrangement of Faraday's disc dynamo, 1831.

A year later, at Ampere's suggestion, a simple commutator was added to convert the output to DC current. This was in the form of a reversing switch driven by the moving part of the machine and thus can be considered as the forerunner of the multi-segment, modern commutator of DC machines. However, since 1837, when Devenport claimed the first patent for the invention of the first radial-flux machine (RFM), it became the accepted configuration for most conventional electrical machines [2].

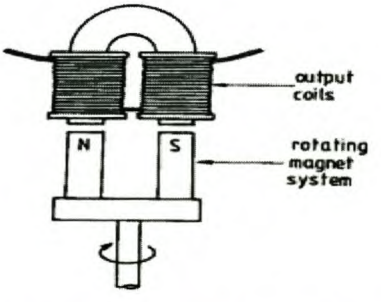

Figure 1.2: The arrangement of Pixii's AC generator, 1831.

Stellenbosch University http://scholar.sun.ac.za

One major drawback of the AFM was the axial attracting forces between the rotor magnets. In the case of the RFM the attracting forces along the airgap perimeter cancel one another. The mechanical reinforcement required in the structure of AFMs, lead to a penalty in machine cost and weight. However, advantages such as the flat shape, smooth rotation with zero cogging and the possibility of high-speed operation lead to a sustained interest in AFM technology today. It is found to be very advantageous in applications such as automobile-radiator cooling-fan motors, electric-vehicle traction motors and in wind turbine generators [3, 4, 5] and [6].

There are several motors commercially available today, based upon the AFPM machine arrangement, that has a disc shaped armature as described in a 1971 British patent [7]. In 1974, Campbell [8] developed the basic theoretical principles of an AFPM machine, which are applicable to the design of all types of axial flux machines in general. The improvements on high field density, rare-earth permanent magnet (PM) materials and power electronic switching devices have largely contributed towards the increasing interests in AFPM machines technology. The use of electronic power switching devices such as IGBTs, contributed to the new topology of the brushless AFPM machine [9]. This new topology proved to be more efficient due to the elimination of commutator related losses.

More recently, Carrichi et al. [10, 11] proposed a water-cooled AFPM for an in-wheel motor application, which benefits from the AFPM machine's features of high compactness and lightness. The AFPM machines are found to be able to deliver power at relatively high frequencies with acceptable voltage regulation. They also had a negligible armature reaction as a consequence of the very low machine inductances resulting from the ironless arrangement of the stator windings.

1.1 Machine topologies and applications.

Single- or double-stage AFPM machines have a disc-type topology with magnets mounted on the rotor discs as shown in Figure 1.3. The magnets can be either surface mounted or buried in the rotor disc. The buried magnets prove to be more

Stellenbosch University http://scholar.sun.ac.za

advantageous in achieving a very compact structure, whilst surface mounted magnets cause fan-effects in the machine, which provide good air circulation in the machine.

High-energy product permanent magnets, such as NdFeB magnets, are used to compensate for the huge airgap between the discs. The use of the permanent magnets instead of field windings improves efficiency due to the absence of field copper losses in the rotor.

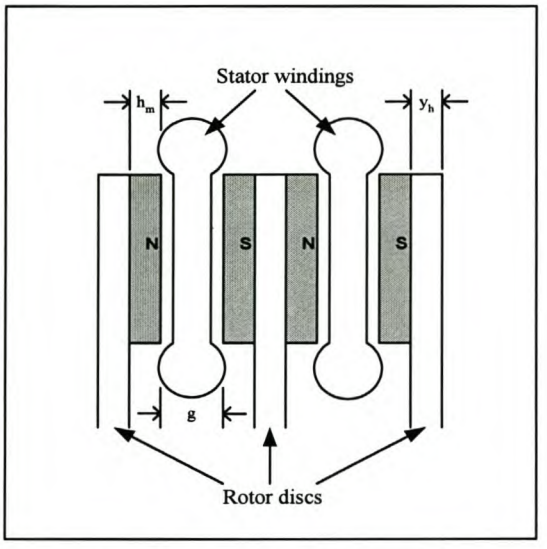

Figure 1.3: Double-stage AFPM machine topology.

The use of iron-less stators improves the efficiency due to the elimination of core losses. It also enhances the cooling process because free-air easily circulate in the gaps left in the stator. One of the major disadvantages of these types of machines is the inability to fill up the stator active area with copper conductors in order to have a higher torque per loading. The stator active area runs radially from the inner radius, r_i, to the outer radius, r_o, of the magnets. It is thus only possible to fill up the space available for copper conductors at the inner radius r_i. As a result thereof, the maximum torque per loading or power output of an AFPM machine is effected by the radius ratio, $\frac{r_o}{r_i}$, which is shown by Campbell [8] to be an optimum when $\frac{r_o}{r_i} = \sqrt{3}$.

An example of an AFPM machine stator, filled with coils, is shown in Figure 1.4.

Stellenbosch University http://scholar.sun.ac.za

1.2 Problem statement

AFPM machines are found to have good features like compactness and lightness when compared to conventional machines. One major challenge is found to be the structural layout of the stator and rotor of the machine, which then determines whether one would exploit those good features of the machine. It often happens that unnecessary weight is added to the machine to increase the mechanical strength of the structure, or to use certain materials which are cheaper than using other lighter materials of the same strength.

This study is a continuation of the work previously done by Lombard [12, 13] on the design of an AFPM machine. Thermal tests were conducted on Lombard's 10 kW prototype machine, which is shown in Figure 1.6. The stator winding and a rotor disc are shown in Figures 1.4 and 1.5 respectively.

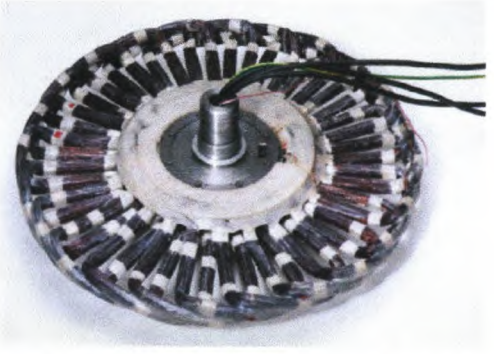

Figure 1.4: Stator winding of a 10 kW prototype AFPM machine [12].

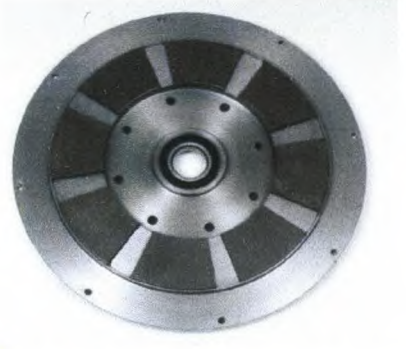

Figure 1.5: Rotor disc of a 10 kW prototype AFPM machine [12].

Stellenbosch University http://scholar.sun.ac.za

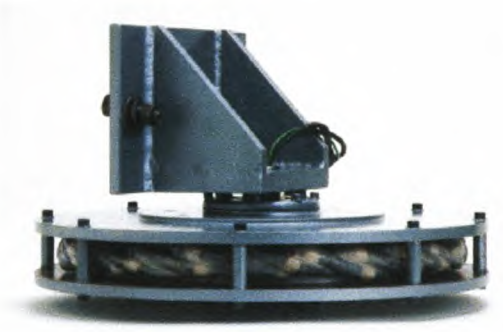

Figure 1.6: The 10 kW prototype AFPM machine of Lombard [12].

It was found necessary to further investigate the behaviour and performance of the AFPM machine at higher output power levels and with a double stator winding arrangement. Since there is a need from the industry for the development of a 300 kW generator that is going to be driven by a heat-engine, a 300 kW output level was then decided on for the AFPM generator (AFPMG). Figure 1.7 shows a block diagram of an AFPMG system, with the 300 kW AFPMG connected to a rectifier and filter.

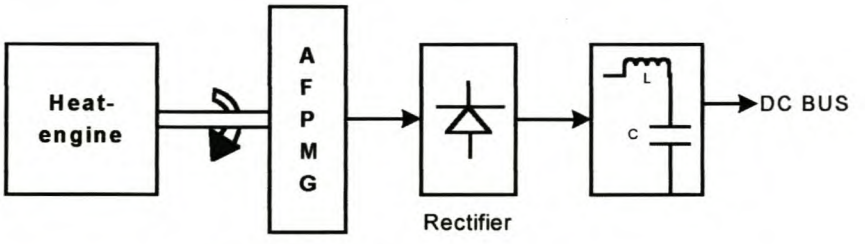

Figure 1.7: System block diagram.

1.3 Approach to problem

It was found by Lombard [12] that due to the large airgap of the AFPM machine, both the lumped circuit method (LCM) and finite element method (FEM) could be used to accurately calculate the peak airgap flux density. Thus, the LCM design approach is used in this thesis to obtain the machine's magnetic operating point. From this the optimum design of the machine is done and the machine parameters are calculated.

Since the outer radius varies with the power output of the machine, it was expected that the machine will have a large diameter at a 300 kW power level. The approach to solve this is to use a double stage arrangement with a reduced outer diameter and with an axial length that is still very short.

Stellenbosch University http://scholar.sun.ac.za

The approach followed with the thermal design, was to conduct thermal experiments on the AFPM machine designed by Lombard [12]. The results obtained were then used in the thermal design of the 300 kW AFPM machine to obtain the optimum machine dimensions that will result in sufficient air-cooling.

1.4 Thesis layout

Chapter 2 of this thesis covers the design of the AFPM machine with some derivations of the design formulae. Chapter 3 deals with the design optimisation and the calculation of the machine parameters. Chapter 4 covers the mechanical design. The machine performance evaluation is discussed in Chapter 5 and the conclusions and recommendations are given in Chapter 6.

Stellenbosch University http://scholar.sun.ac.za

2. AFPM MACHINE DESIGN

This chapter deals with the electrical design of the AFPM generator. The magnetic design is done by means of the LCM and the design equations are presented.

2.1 Magnetic design

The magnetic field distribution in the AFPM machine is one of the important features of the machine and should properly be taken care of in order to optimise the performance of the machine. Figure 2.1 shows a flat layout of the double stage AFPM machine to be designed.

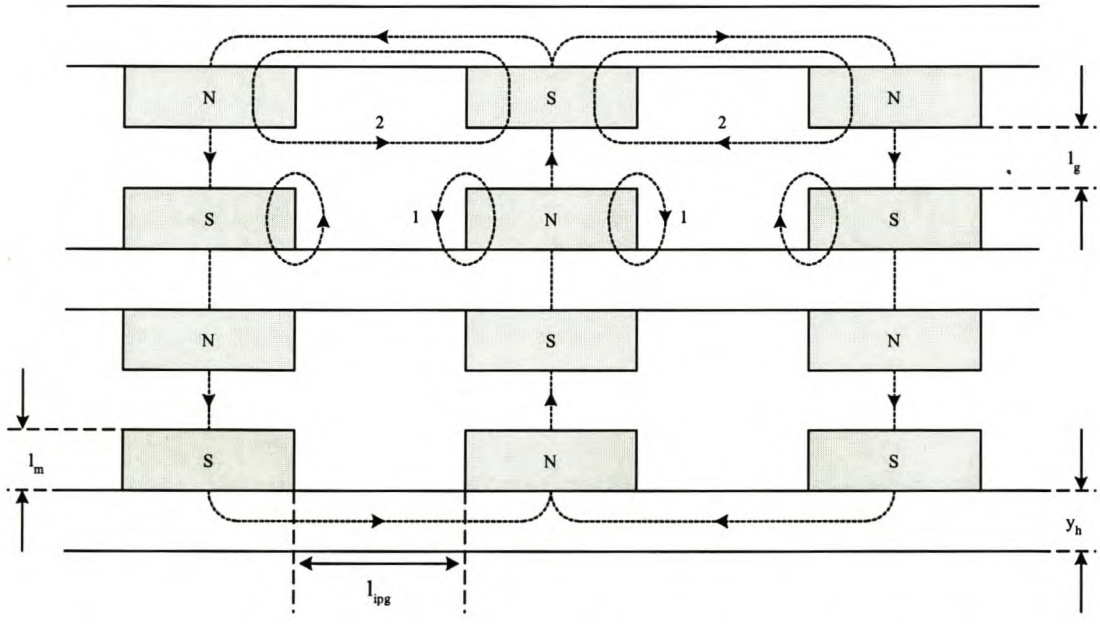

Figure 2.1: Flat model of double stage AFPM machine showing fluxes and dimensions.

It is desirable to have all the flux following the main flux path, which is from one magnet pole through the airgap towards another magnet pole and then back through the back plate. One can minimise the leakage fluxes by imposing the criteria given in (i) and (ii) below.

(i) $l_g < 2\ l_m$, where l_m is the magnet length in the direction of polarisation and l_g is the airgap length.

(ii) $l_{ipg} > l_g$ where l_{ipg} is the inter-pole gap length.

Stellenbosch University http://scholar.sun.ac.za

These criteria are based on the assumption that the flux will always try to take the shortest possible distance from one polarity to another. Thus, applying criteria (i) and (ii) result in a limited machine leakage flux, which in return is desirable for maximum axial airgap flux.

The LCM method is used to solve for the peak airgap flux density in the middle of airgap between two pole faces. In this design it is assumed that the magnetic flux density is uniform over the entire pole face of the magnet. The magnetic circuit of the machine is given in Figure 2.2 below.

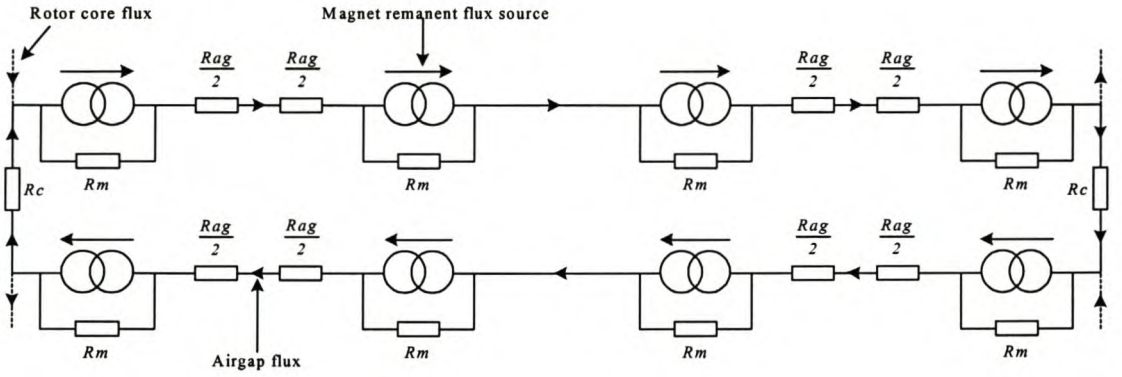

Figure 2.2: Lumped circuit model of the double stage AFPM machine.

The permanent magnets are represented by their Norton equivalent circuit comprising a flux source in parallel with a magnet reluctance. Since the purpose of this circuit is to solve for the peak airgap flux density, it is assumed that fringing is negligible by applying criteria (i) and (ii) above. The airgap and pole face areas are then taken to be equal, thus for a round disc machine,

$$A_m = A_{ag} = \left(\frac{\pi - \theta_{ipg}}{p} \right) (r_o^{\,2} - r_i^{\,2}), \tag{2.1}$$

where p is the number of poles, θ_{ipg} is the inter polar angle between the magnets and r_o and r_i are the magnets outer- and inner radii respectively as shown in Figure 2.3.

Stellenbosch University http://scholar.sun.ac.za

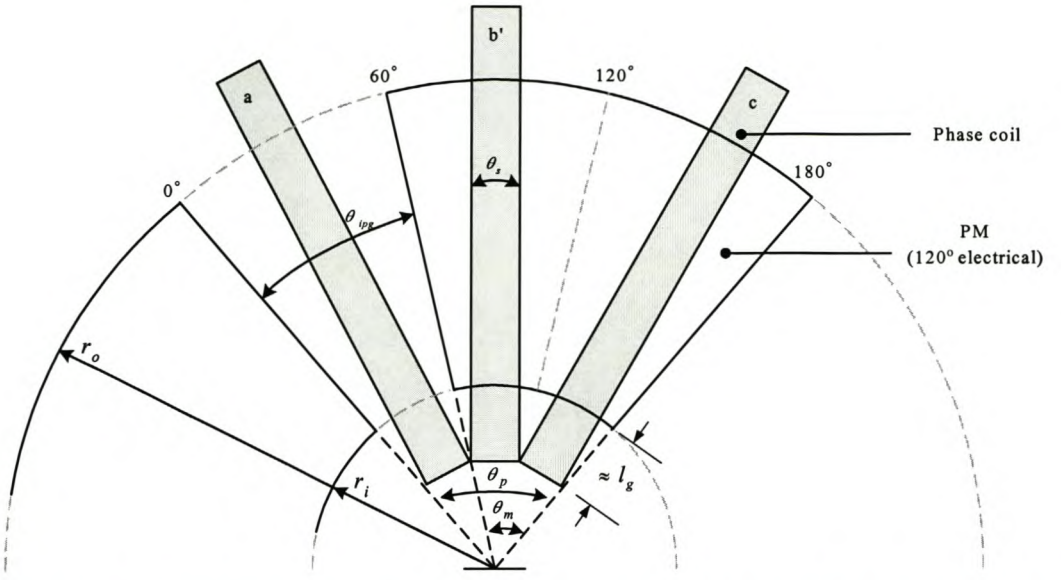

Figure 2.3: Layout and dimensional parameters of AFPM machine showing one pole pitch.

The corresponding magnet and airgap reluctances are formulated below respectively:

$$R_m = \frac{l_m}{\mu_o \mu_{rec} A_m} \tag{2.2}$$

$$R_{ag} = \frac{l_g}{\mu_o A_{ag}}, \tag{2.3}$$

where μ_{rec} is the magnet recoil permeability. The airgap flux is determined by applying an analogy to Kirchhoff's voltage law to the magnetic circuit in Figure 2.1. It can also be seen from symmetry that the rotor core flux is half the airgap flux (φ_{ag}) and thus

$$8F_m = 4R_{ag}\varphi_{ag} + 2R_c\frac{\varphi_{ag}}{2}, \tag{2.4}$$

where F_m is the magnet MMF. The magnet MMF is given by

$$F_m = (\varphi_r - \varphi_{ag})\, R_m, \tag{2.5}$$

where φ_r is the magnet remanent flux. Thus, after combining (2.4) and (2.5) and then solving for the airgap flux it leads to

$$\varphi_{ag} = \frac{8R_m B_r A_m}{8R_m + 4R_{ag} + R_c}$$

UNIVERSITEIT STELLENBOSCH
BIBLIOTEEK

Stellenbosch University http://scholar.sun.ac.za

$$\approx \frac{R_m B_r A_m}{R_m + \frac{R_{ag}}{2}}, \tag{2.6}$$

with $B_r = \frac{\varphi_r}{A_m}$ and with the assumption that the permeability of steel is infinite and thus R_c is negligible. Using the peak airgap flux according to (2.6), the peak torque and peak induced voltage of the machine can be determined.

If one rather considers the MMF drops in one branch and ignores the MMF drops over the rotor iron, the following equation is obtained:

$$2H_g l_g + 4H_m l_m = 0, \tag{2.7}$$

which can be re-arranged in terms of H_g and the absolute value of H_m as

$$H_g = \frac{2|H_m| l_m}{l_g}. \tag{2.8}$$

If it is further assumed that all the flux crosses the airgap, then the following holds:

$$\begin{aligned} B_m = B_g &= \mu_o H_g \\ &= 2\mu_o |H_m| \frac{l_m}{l_g} \end{aligned} \tag{2.9}$$

from equation (2.8). Thus from (2.9)

$$\frac{l_m}{l_g} = \frac{B_g}{2\mu_o |H_m|}, \tag{2.10a}$$

and to satisfy criteria (i), thus,

$$\frac{B_g}{2\mu_o |H_m|} > \frac{1}{2}. \tag{2.10b}$$

B_g thus must be selected such that (2.10b) is satisfied. It is interesting that for N_dF_eB magnets, (2.10b) is satisfied when $B_g > 0{,}5$ T.

2.2 Electrical design of BDC (squarewave) machine.

This section outlines some of the important formulae in the design of a Brushless DC (BDC), AFPM machine. It is called a BDC machine because during conduction the induced phase EMF and phase current are DC quantities. As a result, the back-EMF

Stellenbosch University http://scholar.sun.ac.za

and current waveforms are near squarewave. Since the back-EMF is usually arranged to be trapezoidal, the terms squarewave and trapezoidal are interchangeably used to refer to this type of machine [15]. Due to the symmetry of the double stage case, the equations that are derived are only for one stage.

2.2.1 Mechanism of torque production

For simplicity, the airgap flux density B_g is assumed to be constant over the whole magnet pole face and fringing and leakage fluxes are negligible. The force F_s produced by a single current carrying conductor in the airgap, lying perpendicular to the magnetic field is given by the following:

$$F_s = \int_{r_i}^{r_o} B_g I_s \, dr, \tag{2.11}$$

where I_s is the current in the conductor as shown in Figure 2.4. The resulting torque expression is therefore

$$T_s = \int_{r_i}^{r_o} B_g I_s \, r \, dr = \frac{1}{2} B_g I_s (r_o^2 - r_i^2). \tag{2.12}$$

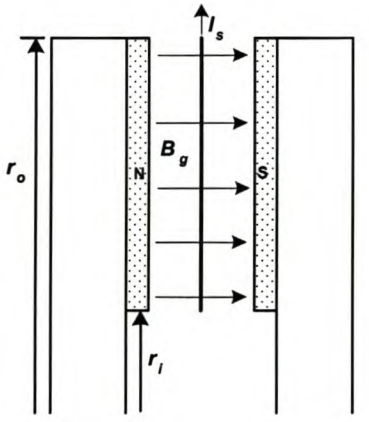

Figure 2.4: Current carrying conductor in a uniform flux density.

Since the active conductor length is defined as $\Delta l = r_o - r_i$ and the average radius as $r_{avg} = \frac{1}{2}(r_o + r_i)$, the torque in (2.12) becomes:

$$T_s = B_g I_s \Delta l \, r_{avg}. \tag{2.13}$$

It can be seen that the total torque can be found if the single conductor current could be replaced with the current in the total number of conductors. This total current is derived in the next section.

Stellenbosch University http://scholar.sun.ac.za

2.2.2 Total electric loading

One major disadvantage of AFPM machines is the impossibility to totally fill the active volume on the stator bore with copper wound coils. It can be seen from Figure 2.3 that the tightest way to place coils on the stator is to have them touch at a radius approximately equal to r_i-l_g (see Figure 2.3). Figure 2.5 gives a simplified layout view of a sector of the machine stator conductors. The maximum area available for the stator conductors at the inner radius is determined by:

$$A_{cu} = 2\pi\,(r_i - l_{e3})t_{cu} \approx 2\pi\,(r_i - l_g)t_{cu}, \tag{2.14}$$

where the end winding length l_{e3} (see Figure 2.6) is approximated with l_g as in Figure 2.3, and t_{cu} is the stator winding thickness as shown in Figure 2.5. The resulting total feeding current for BDC operation (always only two phases active) is then written as

$$I = \left(\frac{m-1}{m}\right) k_f \; J \; A_{cu}, \tag{2.15}$$

where J is the current density, m the number of phases and k_f the filling factor. Substituting for A_{cu} from (2.14), the feeding current becomes

$$I = 2 \; \pi \; J \; k_f \; t_{cu} \left(\frac{m-1}{m}\right)\left(r_i - l_g\right). \tag{2.16}$$

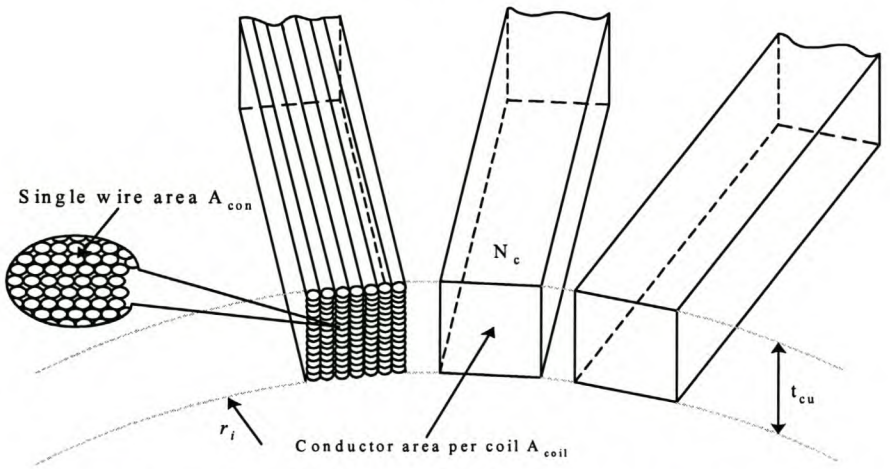

Figure 2.5: Placement of stator coils in AFPM machine.

2.2.3 Torque equation

The machine torque is derived from combining equations (2.13) and (2.16) to yield

$$T = 2\pi\left(\frac{m-1}{m}\right) J\, k_f\, (r_i - l_g)\, t_{cu}\, B_g \Delta l\, r_{avg}. \tag{2.17}$$

Stellenbosch University http://scholar.sun.ac.za

2.2.4 Current equation

The relation between a coil's cross-sectional area A_{coil} and the active copper area of a single conductor A_{con} is given below as (see Figure 2.5)

$$N_c A_{con} = A_{coil} k_f$$
$$A_{con} = \frac{A_{cus} k_f}{N_c}, \tag{2.18}$$

where N_c is the number of turns per coil and k_f is the filling factor. The conductor area per coil in the airgap is given below as

$$A_{coil} = \frac{2\pi(r_i - l_g)t_{cu}}{m\,q\,p}, \tag{2.19}$$

where p is the number of poles, m the number of phases and q is the number of coils per pole per phase. The current in a conductor is given by the following equation

$$I_s = J\,A_{con} = \frac{I_{ph}}{a}, \tag{2.20}$$

where a is the number of parallel circuits and I_{ph} is the phase current. Hence, the phase current is expressed as

$$I_{ph} = a\,J\,A_{con}. \tag{2.21}$$

Substituting (2.18) into (2.21) leads to the following equation

$$I_{ph} = \frac{a\,J\,k_f\,A_{coil}}{N_c}. \tag{2.22}$$

The number of turns in serie per phase, N_{ph}, is given by the following equation

$$N_{ph} = \frac{N_c\,p\,q}{2\,a}, \tag{2.23}$$

which can be re-arranged in terms of N_c. Replacing A_{coil} with (2.19) and using (2.23) equation (2.22) becomes

$$I_{ph} = \frac{J\,k_f\,t_{cu}\,\pi(r_i - l_g)}{m\,N_{ph}}. \tag{2.24}$$

2.2.5 Number of poles

The number of poles, p, in the machine is related to the frequency, f, of the machine as given by the following equation:

$$p = \frac{120\,f}{n}, \tag{2.25}$$

Stellenbosch University http://scholar.sun.ac.za

where n is the speed in rpm. In general, the speed is known in most designs, with the frequency chosen to be a certain maximum. The choice of the number of poles is also dependent on other machine parameters such as r_i and r_o as will become clear later.

It can be observed from Figure 2.3 that each PM pole is separated by an inter-pole gap and that the pole pitch, θ_p, is equal to the sum of the magnet angle, θ_m, and the inter-pole angle, θ_{ip}, that is

$$\theta_p = \theta_m + \theta_{ip}. \tag{2.26}$$

Thus, by defining $k = \frac{\theta_m}{\theta_p}$, it gives

$$\theta_{ip} = \theta_p (1-k) = \frac{2\pi(1-k)}{p}. \tag{2.27}$$

The shortest inter-pole gap length can be written as $r_i\ \theta_{ip}$, and thus (2.27) becomes

$$l_{ipg} = \frac{2\pi r_i (1-k)}{p}. \tag{2.28}$$

Re-arranging (2.28) in terms the number of poles becomes

$$p = \frac{2\pi r_i (1-k)}{l_{ipg}}. \tag{2.29}$$

In order to satisfy the condition for minimized leakage flux (i.e. $l_{ipg} > l_g$), (2.29) is subjected to the following relation

$$p < p_{\max} = \frac{2\ \pi\ r_i (1-k)}{l_g} \tag{2.30}$$

where p_{max} is the maximum number of poles for a given structure.

In BDC machines, one needs 120° of constant flux cutting the phase coil conductors for that time (conduction time). The average angle spanned by a magnet, thus, should be

$$\theta_m \geq 120^\circ + \theta_s, \tag{2.31}$$

where θ_s is the average electrical angle, in degrees, spanned by a phase coil as shown in Figure 2.3. The magnet angle in (2.31) can be rewritten in mechanical degrees as

$$\theta_{mm} = \frac{(\theta_s + 120^\circ)}{p/2}. \tag{2.32}$$

Stellenbosch University http://scholar.sun.ac.za

The width of a phase coil can be approximated by

$$l_s \approx (r_i - l_g)\frac{2\pi}{m\,p} \approx r_{avg}\,\theta_{sm} \tag{2.33}$$

where it is assumed that $q = 1$ and can be re-arranged in terms of the coil span angle in radians as

$$\theta_{sm} \approx \frac{2\pi(r_i - l_g)}{m\,p\,r_{avg}}. \tag{2.34}$$

Changing (2.34) to electrical degrees and substituting into (2.32), then

$$\theta_m = \frac{2\pi}{p}\left(\frac{2}{3} + \frac{r_i - l_g}{m\,r_{avg}}\right) \tag{2.35}$$

in mechanical radians. Since the magnet angle and pole pitch angle is related as

$$\theta_m = k\,\theta_p = \frac{2\pi k}{p}, \tag{2.36}$$

equating (2.36) and (2.35) yields

$$k = \frac{2}{3} + \frac{r_i - l_g}{m\,r_{avg}}. \tag{2.37}$$

This value of k can then be substituted into (2.30) to obtain the maximum number of poles required.

2.2.6 EMF equation

Since it has been assumed that the magnetic flux density distribution is uniform over the entire pole face and of constant value B_g, the induced EMF waveform of a single conductor is ideally rectangular in shape and its peak value can be calculated from the motion voltage equation i.e. the *Blv*-equation. The induced voltage, thus, over an incremental length of conductor is given by the following equation:

$$de = B_g\,v\,dr = B_g\,\omega_m\,r\,dr \tag{2.38}$$

where the rotor linear velocity $v = r\,\omega_m$ and ω_m is the mechanical angular velocity. Expressing equation (2.38) in integral form to represent the total induced EMF over the entire length between inner and outer radius of the magnets becomes

$$e = B_g\omega_m \int_{r_i}^{r_o} r\,dr = \frac{1}{2}B_g\omega_m(r_o^2 - r_i^2) \tag{2.39}$$

and thus simplifying (2.39) yields

$$e = B_g\,\omega_m\,\Delta l\,r_{avg}. \tag{2.40}$$

Stellenbosch University http://scholar.sun.ac.za

The induced phase voltage can then easily be expressed as

$$E_{ph} = 2 N_{ph} e. \tag{2.41}$$

The mechanical angular velocity can be converted to its electrical equivalent by

$$\omega_m = \frac{2\omega_e}{p} = \frac{4\pi f}{p} \tag{2.42}$$

where f is the fundamental frequency of the phase voltages and currents of the machine. Since $f = \frac{n p}{120}$, with n the rotational speed in r/min, simplifying the phase voltage of (2.34) yields

$$E_{ph} = \frac{\pi}{15} n N_{ph} \Delta l \, r_{avg} \, B_g \tag{2.43}$$

2.2.7 Developed power in BDC operation

Since only two phases of a BDC machine are always active, the resulting developed power is given by the following equation:

$$P_{dev} = (m-1) \, E_{ph} \, I_{ph} = T_{dev} \, \omega_m . \tag{2.44}$$

Substituting equations (2.24) and (2.43) into (2.44) the power becomes

$$P_{dev} = \left(\frac{m-1}{m} \right) \frac{J \, k_f t_{cu} \pi^2 (r_i - l_g) n \Delta l \, r_{avg} B_g}{15} . \tag{2.45}$$

Dividing (2.45) with ω_m and replacing n with $\frac{120 f}{p}$, equation (2.12) for the torque of the machine is again obtained.

2.2.8 Phase resistance

The phase resistance of the machine can be easily determined once the length of the conductors is known. Figure 2.6 illustrates the positioning of a stator coil over a pole face and the typical lengths needed for the determination of the total length of the coil conductors.

Stellenbosch University http://scholar.sun.ac.za

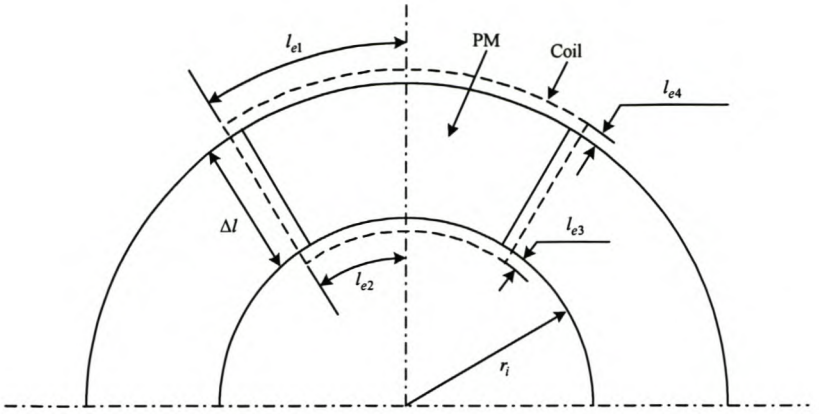

Figure 2.6: Length dimensions of a stator coil.

Assuming symmetry of the coil along the vertical axis, the resistance of half a coil conductor can be written as follows:

$$R_{pc} = \rho_{cu} \frac{\Delta l + l_e}{A_{con}}, \tag{2.46}$$

where ρ_{cu} is the resistivity of copper and l_e the length of half the end-windings. This length is given by

$$l_e = \sum_{i=1}^{4} l_{ei} \,. \tag{2.47}$$

The different end winding lengths contributing to (2.47) can be approximated respectively as follows:

$$l_{e1} \approx \frac{2\pi(r_o + l_{e4})}{2p} \tag{2.48}$$

$$l_{e2} \approx \frac{2\pi(r_i - l_{e3})}{2p}, \tag{2.49}$$

and the lengths l_{e3} and l_{e4} are both approximated by l_g, i.e. $l_{e3} \approx l_{e4} \approx l_g$. Half of the total end winding length, thus, can be written as

$$l_e \approx \frac{\pi(r_o + r_i)}{p} + 2l_g \,. \tag{2.50}$$

The resulting phase resistance can then be re-written as

$$R_{ph} = \frac{2R_{pc}N_{ph}}{a} = \frac{2\rho_{cu}(\Delta l + l_e)N_{ph}}{a\,A_{con}} \,. \tag{2.51}$$

Replacing A_{con} in (2.51) with (2.18) and the resulting A_{coil} with (2.19) respectively, the phase resistance becomes

Stellenbosch University http://scholar.sun.ac.za

$$R_{ph} = \frac{2\rho_{cu} N_{ph}^{\ 2} m(\Delta l + l_e)}{\pi t_{cu} k_f (r_i - l_g)}. \tag{2.52}$$

2.2.9 Machine losses

The AFPM machine losses are almost only resulting from copper and eddy current losses. Since the phase current and resistance have already been defined earlier, the copper losses in the BDC machine are calculated by the following formula:

$$P_{cu} = (m-1)\, I_{ph}^{\ 2}\, R_{ph}. \tag{2.53}$$

The eddy current losses in a round conductor of radius R, resistivity ρ and length λ, and placed in a pulsating magnetic field of peak flux density B and frequency f is given by the following formula [14]:

$$P_e = \frac{\pi^3 B^2 f^2 R^4 \lambda}{2\rho}. \tag{2.54}$$

Since (2.54) was derived for a purely sinusoidal wave, the fundamental flux density component was assumed to be sufficient for this calculation, at the fundamental operating frequency of the machine. The total active length of the conductors is given by $\lambda = n_{cp}\, m\, p\, q\, N_c\, \Delta l$ where n_{cp} is the number of conductors in parallel per phase coil conductor. Rewriting (2.54) in terms of the symbols defined earlier in this thesis for the total eddy current losses gives

$$P_e = \frac{\pi^3 q B_g^{\ 2} f^2 r_{con}^{\ 4} n_{cp} m p N_c \Delta l}{2\rho_{cu}}, \tag{2.55}$$

where r_{con} is the radius of a single parallel conductor in a coil.

The other machine losses are due to bearing and windage losses but their contribution is much lower than the two sources mentioned above.

2.3 Electrical design of sinewave AFPM machine.

The differences between the sinewave AFPM machine and the squarewave AFPM machine discussed in section 2.2, are that the sinewave AFPM machine has

- a sinusoidal flux distribution of magnet flux in the airgap rather than rectangular,
- a sinusoidal phase current waveform rather than rectangular and

Stellenbosch University http://scholar.sun.ac.za

- a sinusoidal distribution of the stator conductors rather than concentrated [15].

Due to the fact that the current and flux density waveforms in sinewave machines are not purely sinusoidal, the design in this thesis is based on the fundamental component only of the waveforms. Some of the equations in this section are directly linked to those in the previous section.

2.3.1 Induced phase voltage

The induced EMF voltage waveform in the sinewave AFPM machine depends partially on the airgap flux distribution, which should be as near as possible to a sinewave, and partly on the winding distribution. The ratio of the magnet pitch over the pole pitch in these machines is generally chosen as $k = \frac{2}{3}$. Figure 2.7 shows the induced voltage in a coil of the sinewave machine with $k = \frac{2}{3}$, the flux density waveform a square wave as shown in Figure 2.8 and $\theta_s = \frac{\pi}{3}$.

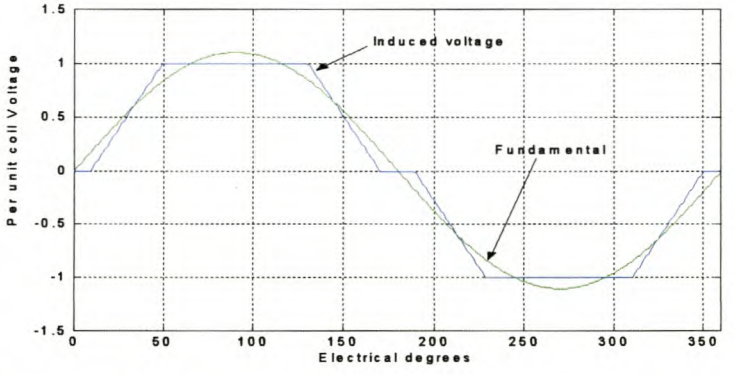

Figure 2.7: Typical induced voltage per coil of the sinewave machine.

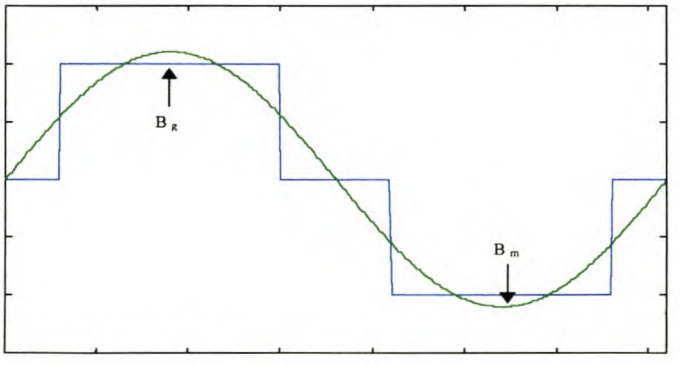

Figure 2.8: Real and fundamental airgap flux density waveform with k=2/3.

Stellenbosch University http://scholar.sun.ac.za

Since the induced voltage is linked to the airgap flux density, the fundamental of the induced voltage must also be linked to the fundamental of the airgap flux density shown in Figure 2.8. The ratio between B_m and B_g of Figure 2.8 can be calculated as follows:

$$B_m = \frac{1}{\pi}\sqrt{2}\sqrt{6}\,B_g$$

$$\approx 1{,}1\;\; B_g . \tag{2.56}$$

Figure 2.9 below shows one pole pitch and the magnet pole area of a p-pole AFPM machine.

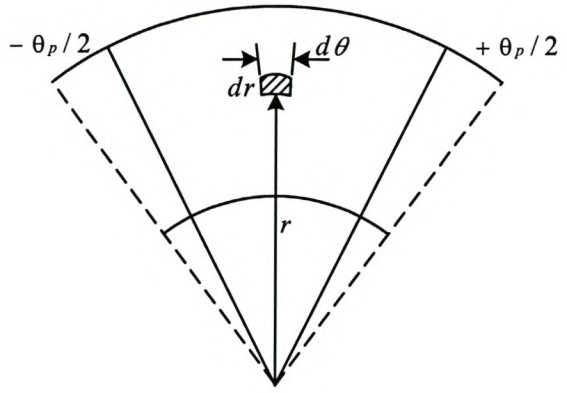

Figure 2.9: Pole pitch and magnet pole area.

Considering Figures 2.8 and 2.9, the flux per pole in the machine with the fundamental airgap flux density is derived as follows:

$$\varphi_p = \int_{-\frac{\pi}{p}}^{\frac{\pi}{p}} \int_{r_i}^{r_o} B_m \cos(\tfrac{p}{2}\theta)\, r\, dr\, d\theta$$

$$\varphi_p = \int_{-\frac{\pi}{p}}^{\frac{\pi}{p}} B_m \cos(\tfrac{p}{2}\theta)\, d\theta \int_{r_i}^{r_o} r\, dr$$

$$= \frac{1}{2}(r_o^{\,2} - r_i^{\,2}) \int_{-\frac{\pi}{p}}^{\frac{\pi}{p}} B_m \cos(\tfrac{p}{2}\theta)\, d\theta$$

Stellenbosch University http://scholar.sun.ac.za

$$= \frac{4}{p} B_m \, \Delta l \, r_{avg} . \tag{2.57}$$

Substituting equation (2.58) in (2.59) gives

$$\varphi_p = \frac{4{,}4}{p} B_g \, \Delta l \, r_{avg} . \tag{2.58}$$

Figure 2.10 below depicts the motion of a phase coil over one magnet pole of the machine.

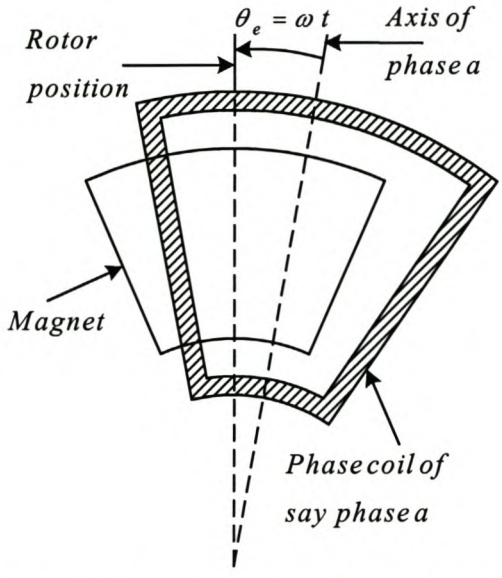

Figure 2.10: Phase coil and magnet pole.

The variation of flux linkage with time of a phase coil is given by:

$$\lambda_{ph}(t) = N_{ph} \, \varphi_p \cos(\omega t) \tag{2.59}$$

where $\omega = 2\pi f$, N_{ph} the number of series turns per phase and φ_p is given by (2.58). Thus, from Faraday's law the voltage induced in a phase is

$$e(t) = \frac{d\lambda}{dt} = N_{ph} \cos(\omega t) \frac{d\varphi_p}{dt} - N_{ph} \, \varphi_p \omega \sin(\omega t) . \tag{2.60}$$

Since in a permanent-magnet machine, $\frac{d\varphi_p}{dt} = 0$ and if one assumes no flux variations due to armature reaction then (2.60) becomes

$$e(t) = N_{ph} \, \varphi_p \, \omega \sin(\omega t) . \tag{2.61}$$

Substituting (2.58) in (2.61) gives

$$e(t) = 2\pi f \, N_{ph} \frac{4\sqrt{12}}{\pi p} B_g \, \Delta l \, r_{avg} \sin(\omega t)$$

Stellenbosch University http://scholar.sun.ac.za

$$= \frac{8\sqrt{12}}{p} f N_{ph} B_g \Delta l r_{avg} \sin(\omega t). \tag{2.62}$$

Thus, the RMS induced voltage can be given as

$$E_{rms} = \frac{8\sqrt{6}}{p} f N_{ph} B_g \Delta l r_{avg} \tag{2.63}$$

Due to the conductor distributions in a coil on the stator bore, the corresponding induced voltages therein are not in phase, but are displaced from each other by a certain angle. For (2.63) thus to be more correct, a distribution factor should also be incorporated, but in this thesis it is neglected. Rewriting (2.63) in terms of $f = \frac{n p}{120}$ yields

$$E_{rms} = \frac{n\sqrt{6}}{15} N_{ph} B_g \Delta l r_{avg}. \tag{2.64}$$

2.3.2 Number of poles

From (2.30) the maximum number of poles in a machine with a *2/3* pole pitch is given by the following formula:

$$p_{\max} = \frac{2\pi r_i}{3 l_g}. \tag{2.65}$$

2.3.3 Current equation

The derivation of an equation for the RMS phase current of the sinewave AFPM machine is the same as that for the BDC machine, but in RMS quantities. Thus, from (2.24) for the sinewave AFPM machine

$$I_{rms} = \frac{J_{rms} k_f t_{cu} \pi (r_i - l_g)}{m N_{ph}}. \tag{2.66}$$

2.3.4 Torque equation

The developed torque for motor operation, where E_{rms} and I_{rms} are as defined earlier in (2.64) and (2.66) respectively, can be determined as follows

Stellenbosch University http://scholar.sun.ac.za

$$T_d = \frac{m E_{rms} I_{rms}}{\omega_m}$$

$$= \frac{m E_{rms} I_{rms}}{4\pi f / p}$$

$$= \frac{m p 8\sqrt{6} f N_{ph} B_g \Delta l r_{avg} J_{rms} k_f t_{cu} \pi (r_i - l_g)}{p 4\pi f m N_{ph}}$$

$$= 2\sqrt{6} B_g \Delta l r_{avg} J_{rms} k_f t_{cu} (r_i - l_g). \quad (2.67)$$

If it is assumed that the RMS current density in the BDC machine is equal to the one in the sinusoidal machine ($J_{rms(ac)} = J_{rms(BDC)}$), then

$$T_{BDC} = 1{,}1 T_{\sin ewave}. \quad (2.68)$$

2.3.5 Power equation

The power output of the sinewave AFPM machine as generator is given by the following equation at unity power factor:

$$P_{out} = m E_{rms} I_{rms}, \quad (2.69)$$

where E_{rms} and I_{rms} are as defined earlier in (2.64) and (2.66) respectively.

2.3.5 Machine losses

The machine losses in a sinewave machine are almost only from the copper and eddy current losses. The copper losses are given by

$$P_{cu} = m R_{ph} I_{rms}^2. \quad (2.70)$$

The equation for the eddy current losses is as given by equation (2.55) for using the same type of conductor arrangement.

2.4 Material consumption

One of the important objectives for the optimisation of PM electrical machines is to minimise the cost of active material, while ensuring rated power and good efficiency [16]. In the following analysis, formulae are derived for calculating the volume and mass of the different parts of the AFPM machine.

Stellenbosch University http://scholar.sun.ac.za

2.4.1 Permanent magnets

The volume of a magnet in this analysis is given by the following equation:

$$V_{mp} = \frac{\pi(r_o^{\,2} - r_i^{\,2})\theta_m l_m}{p\,\theta_p} = \frac{\pi k(r_o^{\,2} - r_i^{\,2})\, l_m}{p}. \tag{2.71}$$

Thus, the total magnet volume of a j stage machine with $(2\,p)$ magnet pieces per stage is

$$V_m = j\,2\,p\,V_{mp} = 2\pi\, j\, k(r_o^{\,2} - r_i^{\,2}) l_m \tag{2.72}$$

and the resulting mass is then given by

$$M_m = \rho_m V_m = 2\pi\, j\, k\, \rho_m (r_o^{\,2} - r_i^{\,2}) l_m, \tag{2.73}$$

where ρ_m is the magnet density.

2.4.2 Rotor yokes

The rotor yoke is the part of the AFPM machine that provides the return path for the magnetic flux to the airgap. For different stages of an AFPM machine arrangement, with j being the number of stages ($j = 1, 2, 3....$), the number of yokes is $(j+1)$. The volume of one yoke is

$$V_{1y} = \pi(r_o^{\,2} - r_i^{\,2}) t_y, \tag{2.74}$$

where t_y is the yoke thickness. Thus, rewriting (2.74) to represent AFPM machines with any number of stages yields

$$V_y = \pi(j+1)(r_o^{\,2} - r_i^{\,2}) t_y \tag{2.75}$$

and the resulting mass is given by

$$M_y = \rho_y V_y = \pi \rho_y (j+1)(r_o^{\,2} - r_i^{\,2}) t_y \tag{2.76}$$

where ρ_y is the yoke steel density .

2.4.3 Stator copper

The volume of only the copper conductors that occupy the available copper area on the stator of the AFPM machine per stage is given by

$$V_{cu} = m\,q\,p\,k_f A_{coil}(\Delta l + l_e), \tag{2.77}$$

Stellenbosch University http://scholar.sun.ac.za

where the coil area, A_{coil}, and the end winding length, l_e, are calculated according to (2.19) and (2.50) respectively. The resulting copper mass for j stages is then given by

$$M_{cu} = j\rho_{cu}V_{cu} = j\rho_{cu}mqpk_f A_{coil}(\Delta l + l_e), \tag{2.78}$$

where ρ_{cu} is the density of the copper. The total airgap (active) volume of the stator winding, thus not including the end-winding volume, but including the epoxy and the gaps between stator coils, is given by

$$V_{ag} = \pi(r_o^2 - r_i^2)t_{cu}. \tag{2.79}$$

2.5 Thermal considerations

The stator windings, rotor magnets and epoxy resins are the most temperature sensitive parts of AFPM machines. As a critical design requirement one should keep their temperatures within specified limits with a large safety margin.

Some thermal measurements were done on a 10 kW laboratory prototype AFPM machine. The results were then used to determine a typical value for copper losses per airgap volume. This value was then used in the design of the double stage AFPM machine, assuming linear relation in terms of cooling. The measured results obtained are shown in Figure 2.11 below.

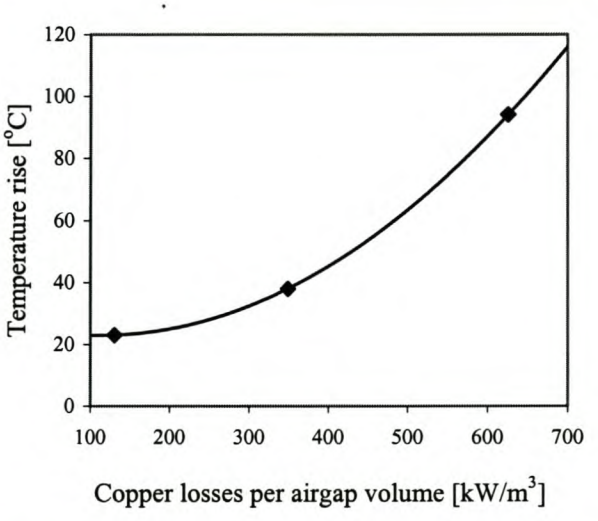

Figure 2.11: Thermal measured results of a 10 kW prototype AFPM machine.

Stellenbosch University http://scholar.sun.ac.za

The measured results shown in Figure 2.11 reveal that the copper loss per enclosed airgap volume should be less than 600 kW/m^3 for a temperature increase of about 90 °C. This was considered as relatively safe since the machine's operating point is limited by the PM grade used of the NdFeB magnets, which tend to demagnetise at temperatures above 150 °C.

Stellenbosch University http://scholar.sun.ac.za

3. DESIGN OPTIMISATION OF AFPM MACHINE

This chapter presents the system specifications and the optimisation of the machine attributes.

3.1 Specifications

The AFPM machine is needed as a generator to operate in the system described in the block diagram in Figure 3.1.

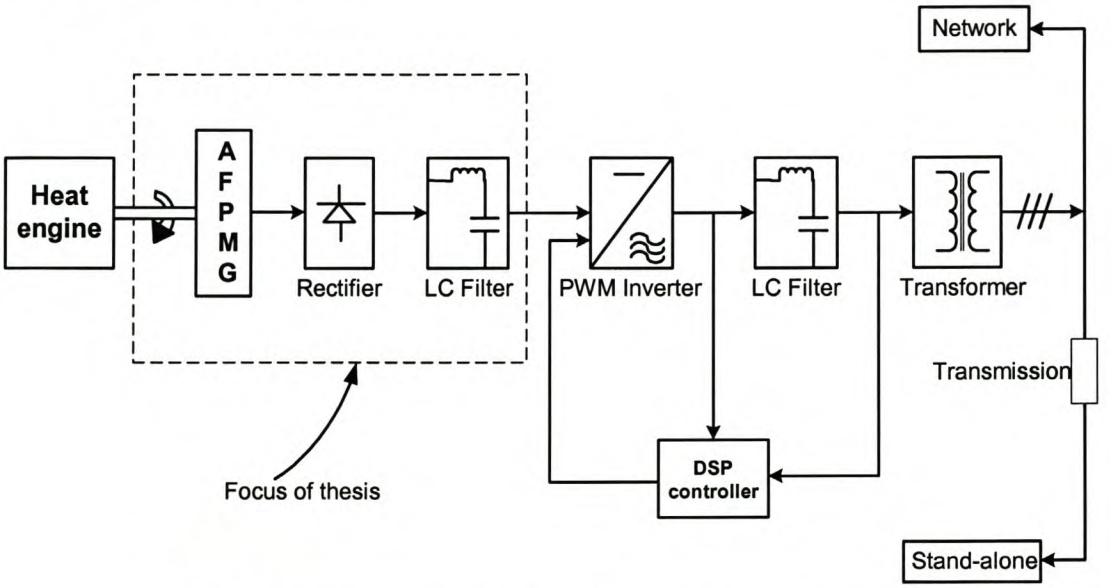

Figure 3.1: Block diagram of a 400 kVA generator system.

The generator system is specified to supply 400 kVA electrical power to a stand-alone load or to the power system network. The specifications of the generator are, therefore, as follows:

- Rated output power: 300 kW at unity power factor;
- Speed range: 2000 to 2500 r/min;
- Phase voltage (RMS): 321 V;
- Phase current (RMS): 444 A;
- Approximate torque range: 1.15 - 1.4 kN.m;
- DC voltage at the terminals of the rectifier: 750 V.

The AFPM generator, thus, must be optimally designed according to these specifications of power, voltage and torque.

Stellenbosch University http://scholar.sun.ac.za

3.2 Maximum torque per loading

The AFPM machine can be optimised for maximum torque per current loading. For both BDC and sinusoidal AFPM machines, the torque can be expressed in general as (from equations (2.17) and (2.67))

$$T = k\,J\,k_f\,t_{cu}\,B_g\,(r_i - l_g)\,\Delta l\,r_{avg}.$$

Rewriting this equation in terms of r_o and r_i, because

$$\Delta l\,r_{avg} = \frac{1}{2}(r_o^{\,2} - r_i^{\,2}), \tag{3.1}$$

yields

$$T \hat{\mathrm{A}} \frac{k}{2} J\,k_f\,t_{cu}\,B_g\,(r_i\,,\ l_g)(r_o^{\,2}\,,\ r_i^{\,2}). \tag{3.2}$$

Taking in the optimum design that r_i and r_o are the only variables in equation (3.2), the torque equation becomes

$$T \hat{\mathrm{A}}\ k_1(r_i\,,\ l_g)(r_o^{\,2}\,,\ r_i^{\,2}) \hat{\mathrm{A}}\ k_1(r_o^{\,2} r_i\,,\ r_o^{\,2} l_g\ '\ r_i^{\,2} l_g\,,\ r_i^{\,3}).$$

For a given r_o, the maximum torque per loading is obtained where the derivative of (3.2) with respect to r_i is zero. Thus

$$\frac{dT}{dr_i} = r_o^{\,2} + 2\,r_i\,l_g - 3\,r_i^{\,2} = 0, \tag{3.3}$$

or else

$$-3r^2{}_i + 2r_i l_g + r_o^{\,2} = 0. \tag{3.4}$$

The two optimum solutions for (3.4) are

$$r_{i1,2} = \frac{1}{3}\left[l_g \pm \sqrt{l_g^{\,2} + 3r_o^{\,2}}\right]. \tag{3.5}$$

From (3.5) with l_g tending to zero, it implies that the optimum r_i for maximum torque per loading appears when

$$r_{i(optimum)} \approx \frac{\sqrt{3}}{3} r_o = 0{,}577\ \ r_o, \tag{3.6}$$

which also agrees with the result found by Campbell [8]. It was calculated that the optimum ratio of inner to outer radius, $r_i\,/r_o$ optimum, varies approximately from 0,577 to 0,75 for large to small AFPM machines, all having the same airgap length. Equation (3.5) is used in the design optimisation with r_o as the variable parameter.

Stellenbosch University http://scholar.sun.ac.za

3.3 Optimisation process

Even though the optimum machine inner radius, $r_{i(optimum)}$, for any given outer radius is already known from (3.5), r_i was varied around the optimum T/J value in order also to optimise other machine parameters such as mass and losses. Two computer programs are developed incorporating the equations derived in Chapter 2 for the BDC and sinewave designs together with the specifications given in section 3.1. These programs are written in Matlab code and are given in Appendix A.

The calculation flow diagrams used for both machine designs are almost similar. The one used for the sinewave AFPM machine is shown in Figure 3.2. In the program it is initially assumed that

$B_g = 0,5$ T;	$B_g/B_y = 0,4$;
$l_g = 10$ mm;	$K_s = 2/3$;
$t_{cu} = 8$ mm;	$k_f = 0,5$;
$l_m = 5$ mm;	$m = 3$;
$q = 1$;	$n_{cp} = 1$;
VR = 7,5%;	$K_s = 1$.

From the design specifications, constants are entered for rated power, displacement power factor, machine rated speed and the rectified DC bus voltage and then also the desired outer radius r_o. The outer radius is used to obtain inner radius values, r_i, at which other parameters of the AFPM machine, such as the losses and active mass, are calculated. For the sinewave machine, the machine RMS phase voltage and fundamental component of the phase current are calculated based on the equations in [10] for 3-phase rectifiers which are given below:

$$\begin{aligned} V_{dc} &= 1,35 V_{LL} \\ I_{RMS1} &= 0,78 I_{dc}. \end{aligned} \tag{3.7}$$

Due to the fact that a value for the determination of machine inductance, L_{ph}, is not yet known the voltage regulation (VR) was used in the calculation of the phase voltage. A typical VR of 7,5 % for AFPM machines was found in literature [11] and is incorporated into equation (3.7) for the calculation of the RMS induced phase voltage E_{RMS} and yields

Stellenbosch University http://scholar.sun.ac.za

$$E_{RMS} = 0,075 \quad \frac{V_{LL}}{\sqrt{3}} + \frac{V_{LL}}{\sqrt{3}} = 1,075 \quad \frac{V_{LL}}{\sqrt{3}} = \frac{1,075 \quad V_{dc}}{1,35 \quad \sqrt{3}}. \tag{3.8}$$

Thus

$$E_{RMS} = 0,46 \quad V_{dc}. \tag{3.9}$$

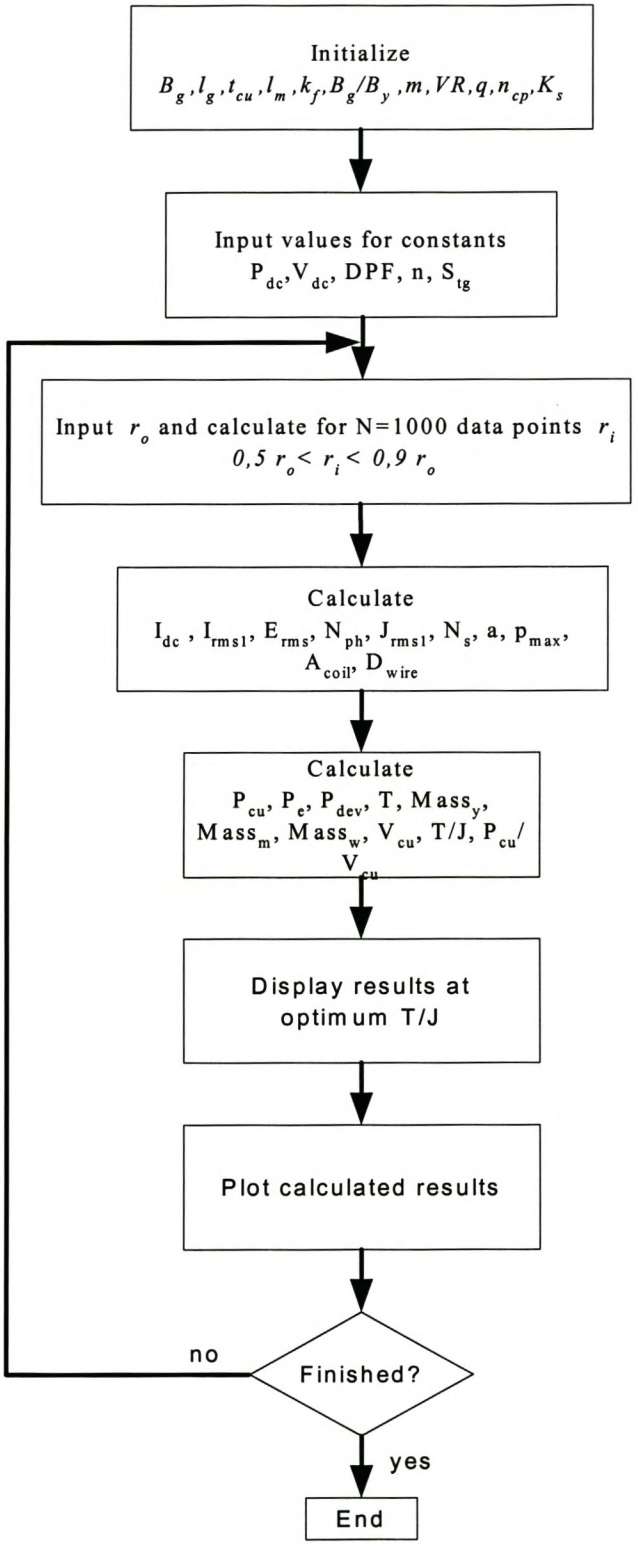

Figure 3.2: Flow diagram of Matlab programs for design of AFPM machine.

Stellenbosch University http://scholar.sun.ac.za

The program then calculates 1000 data points of inner radii, which, together with the outer radius, are used to calculate $K_r=r_i/r_o$ at different r_i values. The results obtained from this is then used in the calculation of N_{ph} and J_{rmsl}, N_s, p_{max}, a, f, A_{con}, A_{coil} and D_{wire}. The machine copper and eddy current losses and mass of active material are also calculated. The calculated results at the point of optimum torque per loading are displayed and the program enables one to view plots of some of the machine parameters. These calculations can then be repeated for machines with different outer radii, until optimum results are attained.

3.4 Design optimisation results

From the thermal considerations in Chapter 2, it is found that a copper loss per volume of less than 600 kW/m^3 is acceptable for natural cooling of an AFPM machine. Calculations are done of machines with different values of r_o, at the same power level and speed, and their characteristics are determined at the point of maximum torque per loading. The results obtained of the copper losses per volume and active mass of the sinewave machine, are plotted versus r_o in Figure 3.3. From this figure one can determine the values of r_o that satisfies the thermal measurement constraint. It can be seen that with an outer radius larger than 330 mm the thermal constraint of less than 600 kW/m^3 is satisfied. To keep the design on the conservative side, but still with the lowest possible mass, a machine with a radius of 340 mm was chosen.

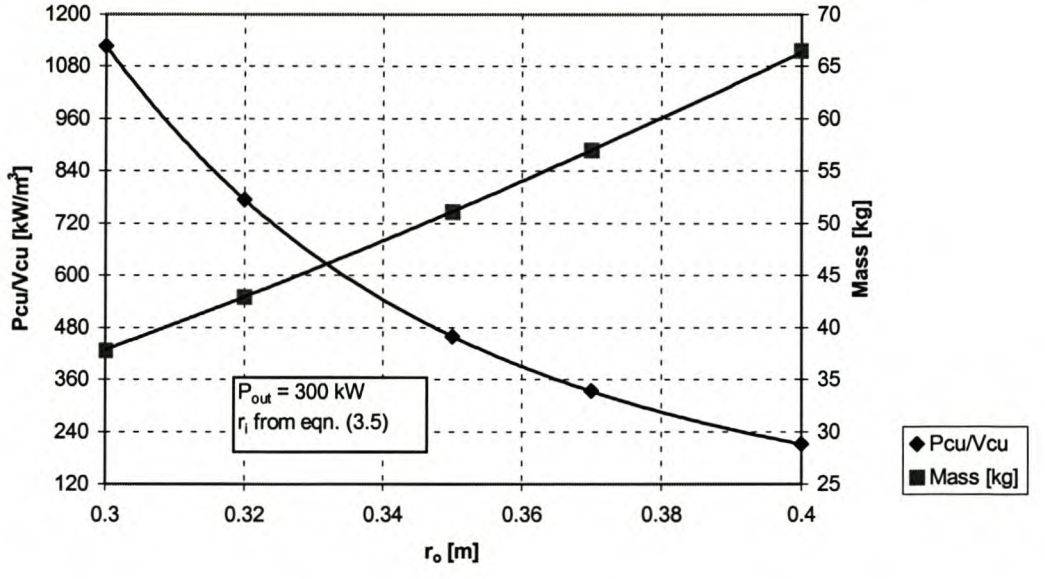

Figure 3.3: Calculated machine copper losses per volume and active mass versus outer radius.

Stellenbosch University http://scholar.sun.ac.za

The optimum results are obtained at the value of r_i for which the torque per loading is a maximum. Figure 3.4 shows a plot of the torque per loading versus radius ratio. It can be seen in Figure 3.4 that the maximum torque per loading for a machine outer radius of 340 mm is at about 0,58, which agrees with the value obtained earlier in equation (3.6). Figures 3.5 to 3.9 give some plots from the design program at the chosen sinewave machine radius. Figure 3.5 shows that the maximum number of poles at a maximum torque per current loading is about 40. The copper losses per stage are shown in Figure 3.6. The copper losses are close to a minimum when the torque per loading is at a maximum, which is favourable.

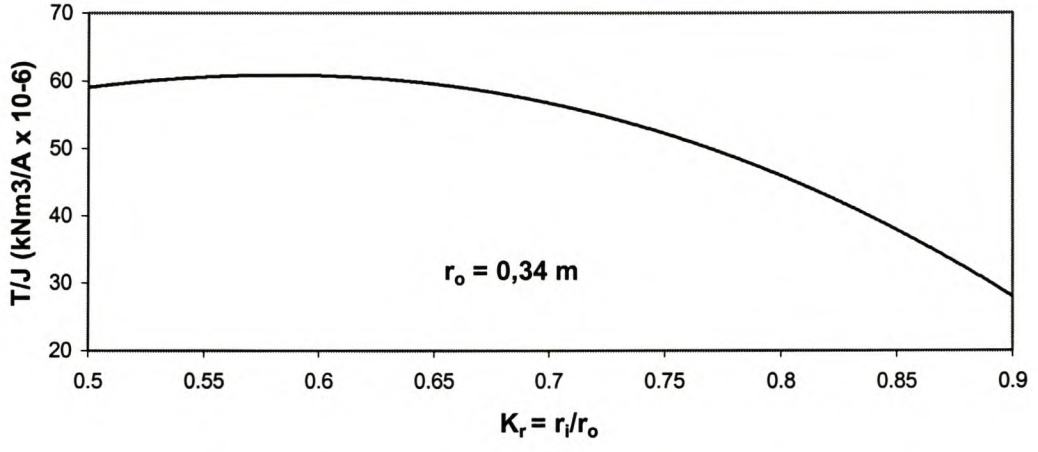

Figure 3.4: Plot of torque per loading versus radius ratio (K_r).

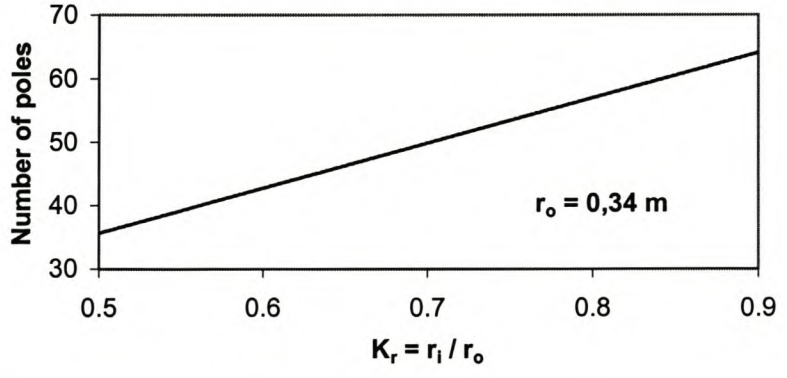

Figure 3.5: Number of poles versus radius ratio ($K_r = r_i/r_o$).

Stellenbosch University http://scholar.sun.ac.za

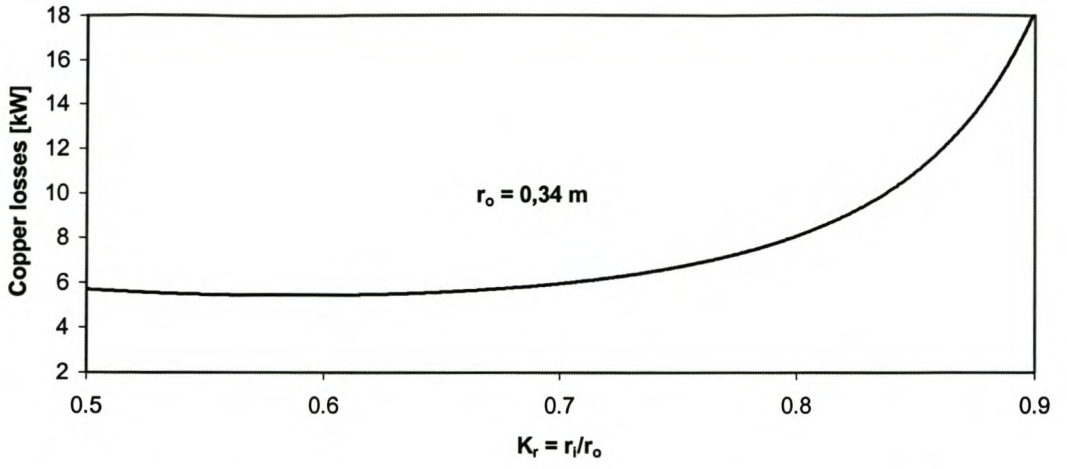

Figure 3.6: Copper losses versus radius ratio ($K_r = r_i/r_o$).

Figure 3.7 shows the eddy current losses for one stage of the AFPM machine. It can be seen that the eddy current loss is relatively high at maximum torque per loading. Thus measures should be taken to take care of these losses. The variation of machine's total active mass with radius ratio is given in Figure 3.8. It can be seen that the total active mass at maximum torque per loading is about 70 kg. The machine's efficiency is also calculated taking into account the copper losses and the eddy current losses as shown in Figure 3.9. It can be seen in Fig. 3.9 that the efficiency at optimum torque per loading is 97,5 %. The maximum efficiency is obtained at a radius of about 0,7, which is much larger than for maximum torque per loading.

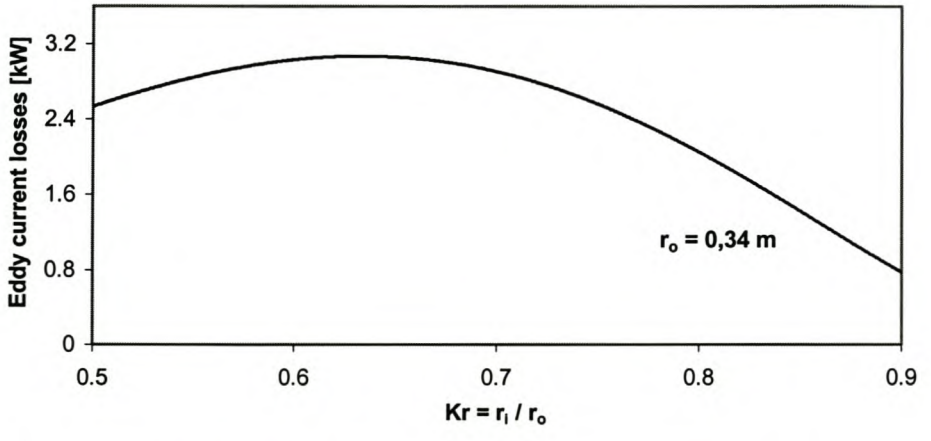

Figure 3.7: Eddy current losses versus radius ratio ($K_r = r_i/r_o$).

Stellenbosch University http://scholar.sun.ac.za

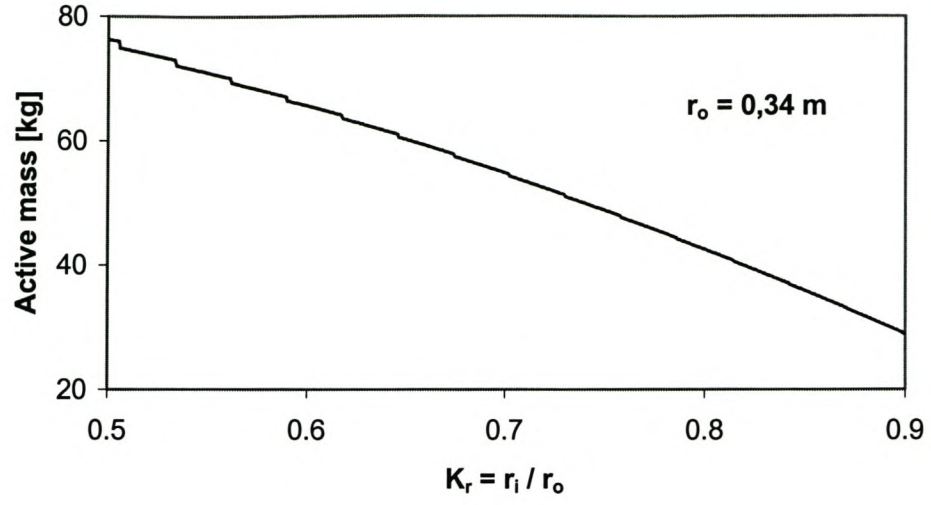

Figure 3.8: Machine mass versus radius ratio $K_r = r_i / r_o$.

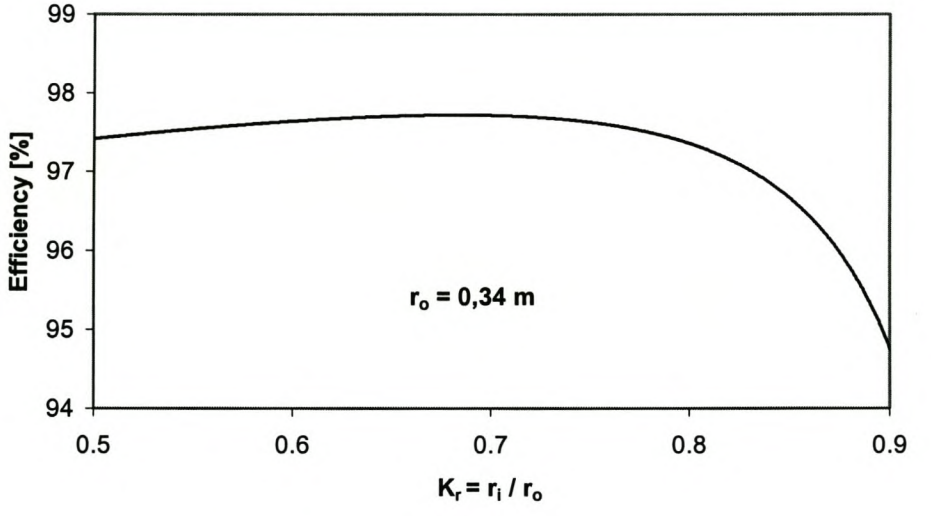

Figure 3.9: Efficiency versus radius ratio $K_r = r_i / r_o$.

3.5 BDC- and sinewave machine design results.

The optimum machine parameters obtained from the sinewave and BDC design programs are tabulated in Table 3.1. It can be seen in Table 3.1 that the two designs differ significantly in the number of poles and yoke thickness. Thus, a quite high power to active mass ratio is obtained for the sinewave design. It was then decided to

Stellenbosch University http://scholar.sun.ac.za

construct and test the lighter sinewave machine, which also looked to be cheaper from a material consumption point of view.

Table 3.1: Design results of BDC- and sinewave machines.

Machine type	BDC	Sinewave
Output power	300 kW	300 kW
Phase voltage	440 V_{peak}	321 V_{RMS}
Line current	364 A_{peak}	360 A_{RMS}
Torque	1368 Nm	1420 Nm
Copper losses	4,4 kW	5,4 kW
Eddy current losses	1,2 kW	2,8 kW
Efficiency	98,2 %	97,6 %
Phase resistance	16 mΩ	12 mΩ
Poles per disc	16	40
Rated Speed	2300 rpm	2300 rpm
Diameter ratio (D_I /D_o)	0,587	0,579
Outer diameter (D_o)	680	680 mm
Pole arc to pitch ratio	0,901	2/3
Magnet thickness (l_m)	5 mm	5 mm
Yoke thickness (t_y)	18,2 mm	6 mm
Airgap length (l_g)	10 mm	10 mm
Current density	11,4 A_p/mm^2	11,5 A_{RMS}/mm^2
Number of turns	50	50
Mass of magnets	17 kg	13 kg/stage
Mass of yoke	34 kg	15 kg/disc
Mass of windings	10 kg/stage	10 kg/stage
Total active mass	152 kg	86 kg
Power / Mass	2,0 kW/kg	3,6 kW / kg

A lumped circuit thermal model analysis was also done by Wang in [17], to predict the thermal behaviour of the 300 kW machine. Table 3.2 shows the predicted temperatures of the 300 kW machine's stator, rotor and PMs. The data presented in Table 3.2 shows that the PMs of the middle disc are quite prone to demagnetisation, because their temperatures are higher than the outer disc PMs. This difference is due to the exposure of the outer disc surfaces to the surrounding ambient air.

Stellenbosch University http://scholar.sun.ac.za

Table 3.2 Predicted temperature distribution of 300 kW machine

Machine part	Temperature (°C)
Middle rotor disc	76
PM on middle disc	75,5
Air flow touching middle disc	69,37
Stator winding	102,34
Air flow touching outer disc	66,27
PM on outer disc	64,38
Outer rotor disc	64,12
Ambient air	24

Stellenbosch University http://scholar.sun.ac.za

4. MECHANICAL DESIGN CONSIDERATIONS

The machine construction and the mechanical design considerations are discussed in this Chapter. It mainly deals with the mechanical FEM simulations on the rotor yoke thickness, to ensure that its mechanical strength can withstand the huge attraction force of the rotor magnets.

4.1 Stator construction

Two identical stators for the two-stage machine are constructed of which each has a three-phase winding. Each phase winding consists of 20 parallel phase coils (see Figure 4.1). Each phase coil consists of 50 turns in series per phase and each phase turn consists of 4 parallel conductors.

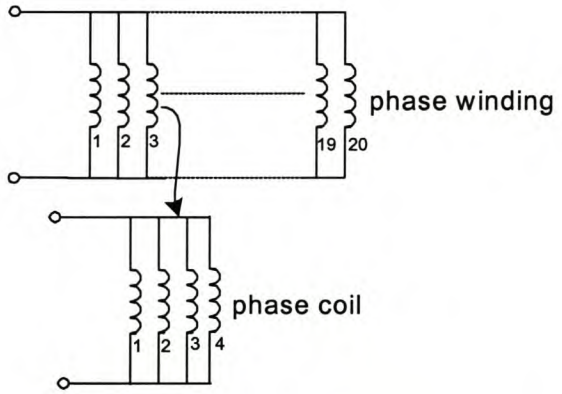

Figure 4.1: Phase coil connection of a stator winding of the AFPM machine.

The phase coils where wound on a trapezoidal shaped former that allow some extra length for the end windings. The end winding length is minimised to reduce the extra copper losses that would otherwise be introduced by them. The end windings of the coils are bent to allow overlapping of the coils as illustrated in Figure 4.2. Some of the phase coils had thermocouples inserted to allow stator temperature monitoring.

There are also studs embedded in the outer part of the stator to enable attachment to the rest of the machine. The positioning and spacing of the phase coils are carefully ensured by means of a mould. To ensure releasing of the stator from the mould, the mould was coated with a thin layer of Vaseline.

Stellenbosch University http://scholar.sun.ac.za

Figure 4.2: View of the stator coils in the former.

The EC 115-R epoxy and EC 336-H hardener are used in conjunction with a West System high-density filler (404) to mould the stators. The products are obtained from Exaton Composites (Pty) Ltd. The filler is selected for maximum strength and hardware bonding characteristics. The mixing ratio used is 100 parts epoxy to 28 parts hardener. The ratio is in parts by weight and should be accurate with maximum 2% error allowable. The coils are entirely embedded in the epoxy mixture at the end windings at the machine inner and outer radii. The remaining parts of the coils, between the end windings, are coated with a low viscosity epoxy mixture to strengthen it (see Fig. 4.3). The stator in the mould is then left to harden for at least 24 hours. The next day, the stator (still inside the mould) is taken for elevated temperature curing in an oven. The curing schedule consists of keeping the stator for 2 hours at each of following temperatures: 60 °C, 80 °C, 120 °C and 160 °C. The typical heat distortion temperature that can be reached is 149 °C, with a tensile strength of 72 kN/mm^2. Figure 4.3 shows the stator after it was cured at elevated temperatures.

Figure 4.3 Stator of the AFPM generator.

Stellenbosch University http://scholar.sun.ac.za

4.2 Rotor construction

The constructed AFPM machine has axially polarized rectangular slab PMs of NdFeB material mounted on the surface of mild steel discs rotors. The PM grade used is N35SH with a remanence of approximately 1,2 T and a coercivity of approximately 903 kA/m. The rotor of the machine consists of the magnets and the back iron plates (mild steel discs). The products used to attach the PMs to the rotor discs are Araldite AV138M epoxy and HV 998 hardener from Ciba-Geigy. The recommended mixing ratio is 100 parts epoxy to 40 parts of hardener (by weight or volume). The mixing ratio is not very sensitive. A former was used to position the magnets on the yoke. Figures 4.4 and 4.5 show the magnets glued to the outer rotor disc and to the middle disc, respectively. A rotor disc magnet has a radial length of 142 mm, stretching from the inner- to the outer radii with a span of 6^{o} and an inter magnet spacing of 3^{o}.

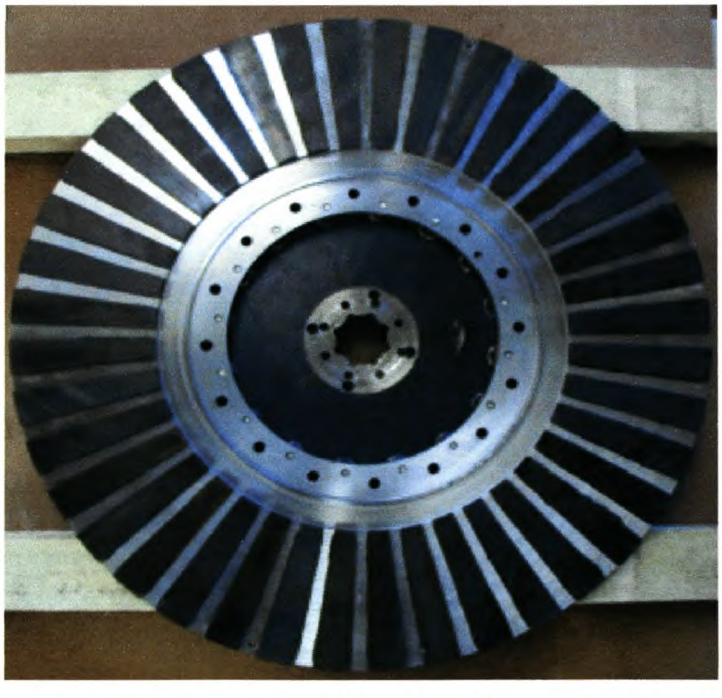

Figure 4.4: Outer rotor disc with magnets.

Stellenbosch University http://scholar.sun.ac.za

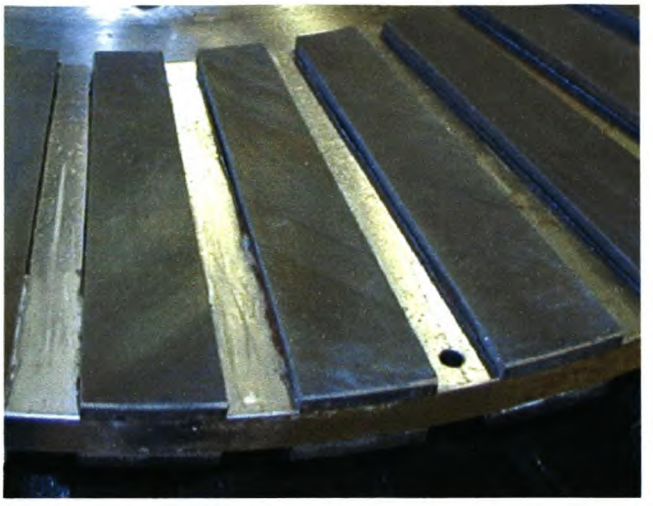

Figure 4.5: Middle rotor disc with magnets.

Since only the outer rotor discs contributes to guiding the flux in a multistage AFPM machine, some trade off between cost and weight has to be applied to the selection of the rotor middle disc. Here one can either consider using aluminium or mild steel, where the difference in cost is about 6 times higher for aluminium per kilogram. Since mass was not very crucial in this design, the cheaper option was selected for the prototype AFPM machine.

The attraction force, F, resulting from placing two magnets a distance g apart, with a each magnet having a surface area A_m and a thickness of h_m, and B_g the air-gap flux density, is approximated by the following equation:

$$F = \frac{2 B_g^{\,2} h_m^{\,2} A_m}{\mu_o g^2} \tag{4.1}$$

The total attraction force calculated between the rotor magnet discs with B_g = 0,5 T, g = 10 mm, h_m = 5 mm and A_m = 0.004 mm^2 is about 16 kN (about 1,6 tons). This huge magnetic attraction force makes the machine assembling difficult. Furthermore, the next section deals with an investigation on the severity of this force on the yoke thickness.

4.3 FE Analysis of magnetic loads on rotor discs

The FE analysis described in this section was done in conjunction with Mr. K. van de Westhuizen from the Department of Mechanical engineering at the University of

Stellenbosch University http://scholar.sun.ac.za

Stellenbosch. The severity of the magnetic attraction force on the rotor yoke and back-plate design is investigated by means of FE analysis. Different options are studied for strengthening the rotor discs in order to counteract the magnetic attraction force.

The structure of the rotor outer steel discs is designed with the help of a mechanical strength FE program. It is important that the deflection of the outer steel discs, due to the axial magnetic loads, is not too severe to close the 1 mm air gap between the permanent magnets and the stator windings. Note that the forces on the centre disc are balanced and will result in negligible deflection there-of. A maximum deflection of 0,5 mm at the outer radius of the discs is allowed, as long as the maximum mechanical stress is within limits. By choosing a small allowable deflection, one also ascertains that the permanent magnets do not experience any excessive forces that can potentially break them or peel them off from the steel disc.

As the two outer disc structures experience the same load, only one of them needs to be investigated. Thus a quarter model is created with 4-node shell-elements and symmetry boundary conditions implemented. A 17,5 kN axial magnetic force (just larger than the 16 kN calculated from eqn. 4.1) is applied in the form of a constant 72,9 kPa pressure load over the total area that the permanent magnets occupy as shown in Figure 4.6. The stiffness provided by the magnets was not included to keep the design on the conservative side.

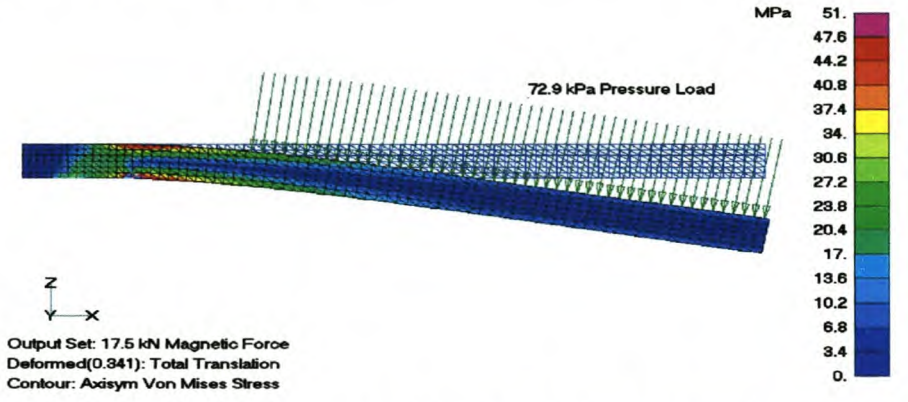

Figure 4.6: Deflection (blown-up) and Von Mises Stress distribution of laboratory prototype modelled with axial-symmetric-elements.

Stellenbosch University http://scholar.sun.ac.za

Since the deflection found from the first simulation was far beyond the allowable margin, a means of strengthening the rotor disc by putting ribs onto its surface was used, as shown in Figure 4.7. The height of the ribs is taken as 20 mm and the rib length from the inner diameter of the steel disc to an outer diameter of 500 mm. There is not much bending beyond a diameter of 500 mm, and therefore there is no need to extend the ribs further towards the outer diameter of the steel discs. The number of ribs used are 0, 8 or 16. The thickness of the ribs and the steel disc were varied to obtain the design with the lowest mass, and with acceptable deflection and stress. Table 2 lists some of the options studied with the mass, deflection and maximum stress given.

Table 4.1: Some of the steel disc options studied.

No. of Ribs	Disc Thickness (mm)	Rib Thickness (mm)	Deflection (mm)	Von Mises stress (MPa)	Mass/Disc (kg)
0	6	-	2,60	207,8	14,3
0	8	-	1,11	116,7	19,1
0	10	-	0,57	74,5	23,8
0	12	-	0,34	51,6	28,6
8	6	8	1,04	149,3	15,4
8	6	10	0,97	129,7	15,7
8	8	8	0,60	109,7	20,2
8	8	10	0,56	96,5	20,5
16	6	8	0,64	90,2	16,6
16	6	10	0,59	76,4	17,2
16	7	8	0,50	81,6	19,0
16	7	10	0,46	69,3	19,5
16	8	8	0,40	73,2	21,4
16	8	10	0,37	62,8	21,9

It can be seen from Table 4.1 that the option with 16 ribs, 10 mm rib thickness and 7 mm disc thickness has the lowest mass (19,5 kg) of all the options with the maximum deflection within limits, that is less than 0,5 mm. The maximum stress of 69,3 MPa is much lower than the typical yield strength of mild steel, that is in the region of 300 MPa. Figure 4.7 shows the deflection (blown-up) and Von Mises stress distribution of

Stellenbosch University http://scholar.sun.ac.za

this 16-rib option. It can be concluded that the maximum deflection, and not the maximum Von Mises stress, influences the decision of the most suitable option.

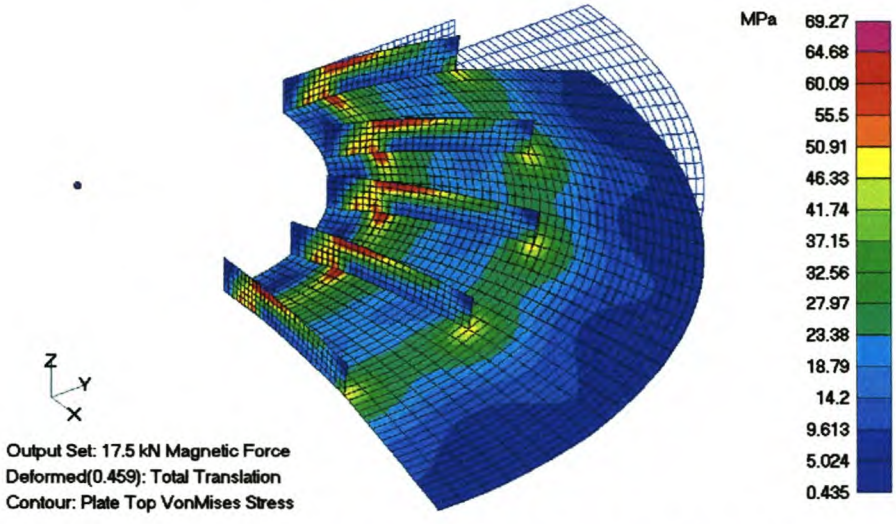

Figure 4.7: Deflection (blown-up) and Von Mises stress distribution of the proposed 16-rib option.

If manufacturing costs are taken into account for small production volumes, it is better to rather use a thicker steel disc with no ribs. The 12 mm disc option in Table 4.1 (with 0 ribs) also satisfies the deflection criterion, but its mass is 9,1 kg more than the 16 rib option. The extra cost of the steel will be much lower than the savings introduced by having ribs. The addition of the ribs will need expensive casting or welding operations. As long as the added mass of the 12 mm option can be tolerated, this option is the best for small production volumes and for laboratory prototypes. Figure 4.8 shows the deflection (blown-up) and Von Mises stress distribution of the laboratory prototype 12 mm option.

An additional Finite Element Model using axial-symmetric-elements was also created for the prototype 12 mm option (Figure 4.8). These results and those obtained with the shell-elements (Figure 4.6) agree well (both analyses gave a maximum displacement of 0,34 mm). Figures 4.6 and 4.8 indicate very clearly that most of the bending of the disc takes place in a very narrow region between the diameter of the support structure and the inner diameter of the magnets.

Stellenbosch University http://scholar.sun.ac.za

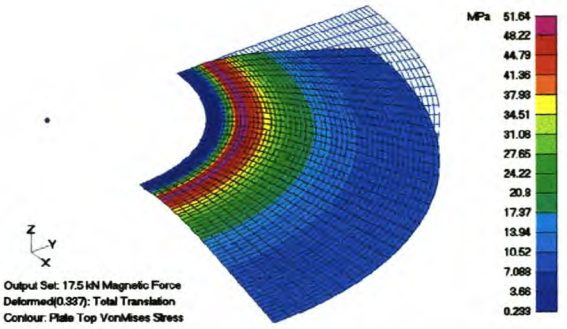

Figure 4.8: Deflection (blown-up) and Von Mises Stress distribution of laboratory prototype disc (12 mm thick with no ribs).

From the electrical design in Chapter 3 the yoke thickness is calculated as 6 mm. Due to the large magnetic attraction force the 6 mm has to be changed to 12 mm to satisfy the deflection criterion. Some of the initial electrical design data given in Chapter 3, thus, has to be changed. The resulting mass per disc and other parameters that change due to the magnetic attraction force between the rotor discs are tabulated in Table 4.2. It can be seen that the magnetic attraction force resulted in a decrease in the power to mass ratio of about 34 % from the electrical design.

Table 4.2: Change of AFPM machine parameters due to magnetic attraction force.

Disc thickness (t_y)	6 mm	12 mm
Mass of yoke	15 kg	28,6 kg
Total mass (active material)	86 kg	129,2 kg
Power / Mass	3,6 kW/kg	2,3 kW/kg

4.4 Assembling of rotor discs

The assembling and disassembling of the AFPM machine is very difficult due to the huge magnetic attraction forces. The forces between the discs make it particularly difficult to position the discs 10 mm apart with a 1 mm clearance between the magnets and the stator windings. This problem is solved by the use of an assembling mechanism, as shown in Figures 4.9 and 4.10, that moves the outer rotor discs towards the middle disc from an airgap spacing of about 100 mm on each side. The rotation of a left- and right hand threaded shaft causes the discs to move precisely the same inwards or outwards with the same airgap spacing. The thread on the shaft provides a blocking mechanism to counteract the attraction force on the outer discs as

Stellenbosch University http://scholar.sun.ac.za

they move axially towards the middle disc. Figures 4.10, 4.11 and 4.12 show the complete AFPM machine during assembling.

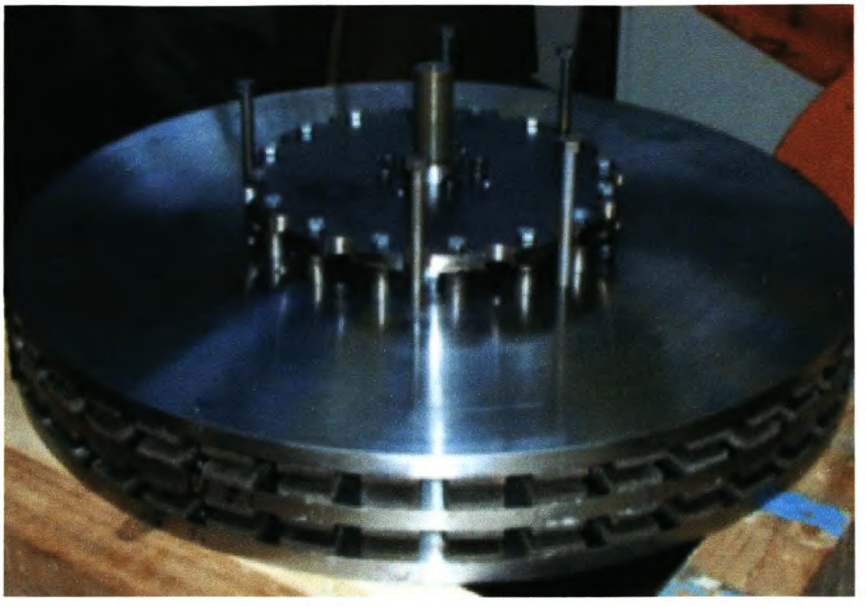

Figure 4.9 Rotor assembling without stator.

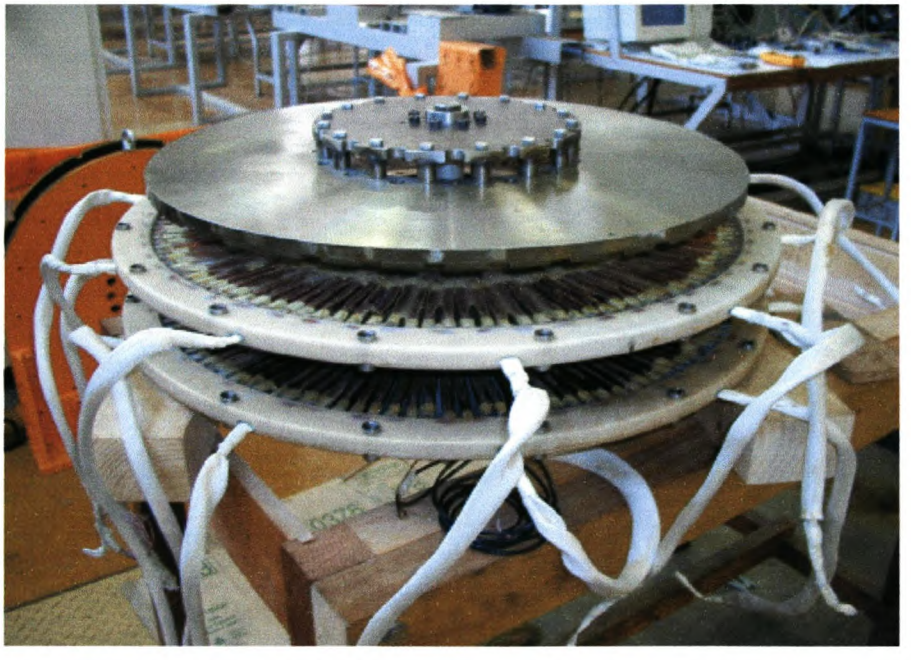

Figure 4.10: Machine assembling with assembly tool shown.

Stellenbosch University http://scholar.sun.ac.za

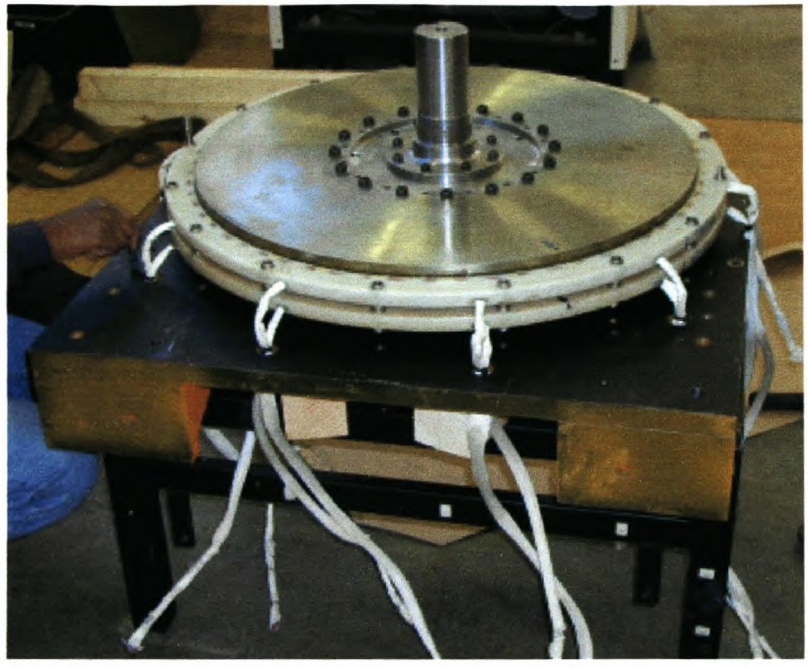

Figure 4.11: Assembly tool removed.

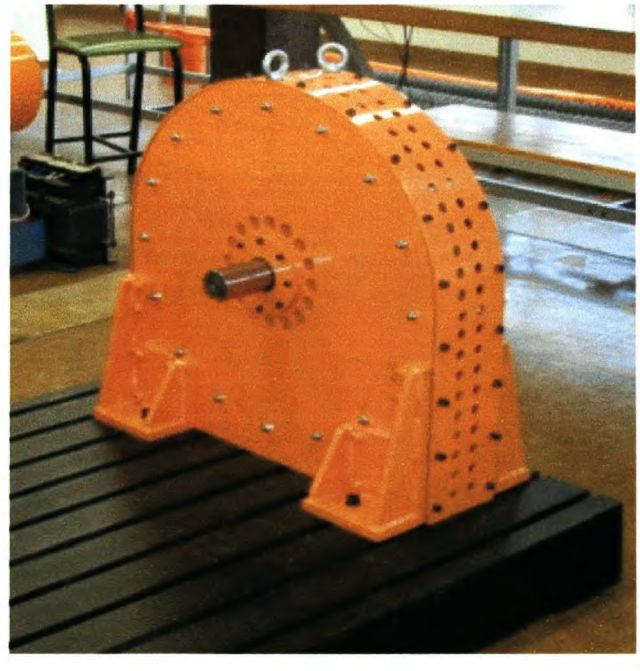

Figure 4.12: AFPM generator assembled.

4.5 Measurements of airgap length between rotor magnets

The AFPM machine was first assembled without the stator winding to measure the space between each pair of magnets on the rotor. Figure 4.13 shows the measured

Stellenbosch University http://scholar.sun.ac.za

results where gaps 1 and 2 are the two airgaps of the double stage machine. It can be seen that the spacing is not uniform 10 mm and that the bottom disc has a minimum spacing of about 9 mm. This variation is assumed to be due to the tolerances of the magnets and the difficulty to ensure that the glue layer thickness is the same on every magnet.

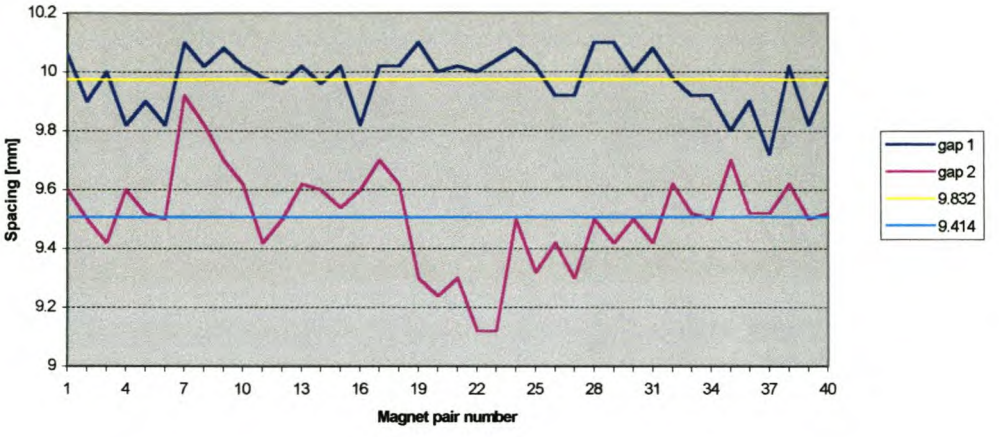

Figure 4.13: Measured spacing between rotor disc magnets

To solve the spacing problem between the discs, it was decided to add shims to ensure that both gaps are on average 10 mm or above. Another measurement was then done and the improved results are shown in Figure 4.14. The deflection of the rotor discs due to the magnetic attraction force is also measured and found to be on average equal to 0,2 mm. This is close to the 0,34 mm from the FE-analysis (Table 4.1). The measured deviation is less, due to the slightly larger average airgaps.

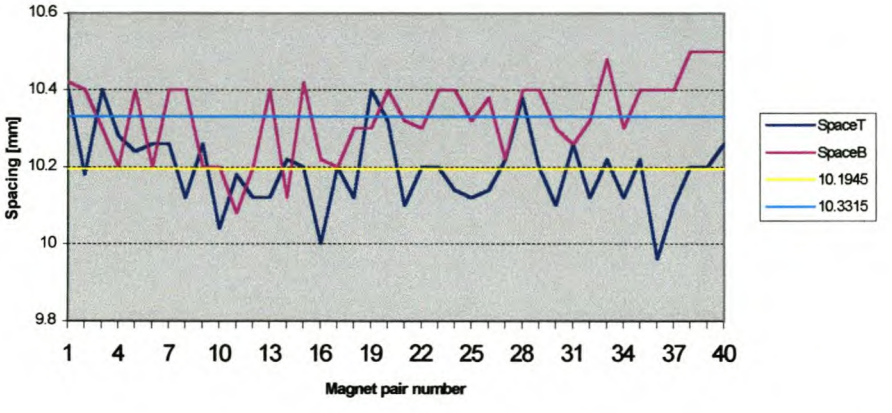

Figure 4.14: Magnet spacing after insertion of shims between rotor discs.

Stellenbosch University http://scholar.sun.ac.za

5. PERFORMANCE OF AFPM MACHINE AS GENERATOR

This chapter deals with the evaluation of the performance of the 300 kW machine as generator. To test the machine in the laboratory, the AFPM machine was driven by an induction machine and its output connected to a rectifier load system as shown in the block diagram of Figure 5.1.

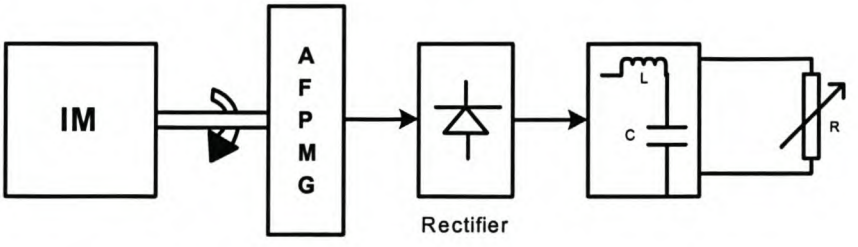

Figure 5.1: Block diagram of the experimental set-up.

5.1 No-load tests

The no-load tests are done on the machine first to compare the wave shapes of the airgap flux density and phase EMF with that predicted by the sinewave AFPM machine design of Chapter 2. Some measurements between the rotor discs of the airgap length and the flux density are also done to determine the possible discrepancies.

The stator is constructed such that each phase winding consists of 20 parallel phase coils, with each phase coil consisting of 50 phase turns. Each phase turn consists of four parallel conductors (see Figure 5.2). The four EMFs (E_{1N}, E_{2N}, E_{3N} and E_{4N}) induced in the parallel conductors with each end of the parallel conductors open circuited, are measured. Furthermore, the circulating currents in the parallel conductors (connected as in Figure 5.2) are also measured.

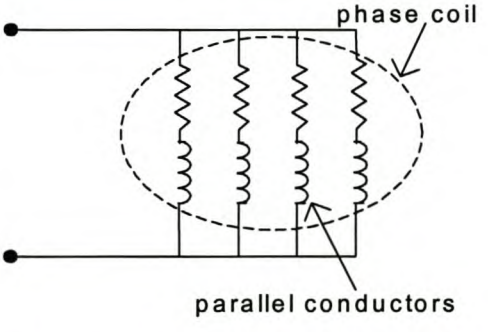

Figure 5.2: Stator phase coil consisting of four parallel conductors.

Stellenbosch University http://scholar.sun.ac.za

It was difficult to measure the eddy current losses to verify the empirical formula used in the machine design (equation 2.55) with all the parallel coils open circuited. However, thermal measurements versus frequency are done to determine the heating effect of the eddy currents.

5.1.1 Airgap flux density waveform and harmonics

To obtain the shape of the airgap flux density, the machine was run at a speed of 1000 rpm and the flux density waveform was measured by means of a small 10 turn coil placed in the machine airgap. The relationship between the flux density and the induced voltage in the test coil can be obtained from (2.39) as

$$e(t) = N \times B_g(t) \times (r_o^{\ 2} - r_i^{\ 2}) \times \omega_m$$

$$\therefore B_g(t) = \frac{e(t)}{N(r_o^{\ 2} - r_i^{\ 2})\omega_m}. \tag{5.1}$$

Thus at 1000 r/min, eqn. (5.1) can be simplified further as

$$B_g(t) = \frac{e(t)}{80{,}6}. \tag{5.2}$$

The measured and the approximated flux density waveforms of the AFPM machine are shown in Figure 5.3.

It can be seen from Figure 5.3 that the approximated flux density is approximately the average of the measured flux density at the plateau. An FFT was done on the measured flux density waveform of Figure 5.3 to determine its harmonic content. The flux density harmonics are shown in Figure 5.4.

Stellenbosch University http://scholar.sun.ac.za

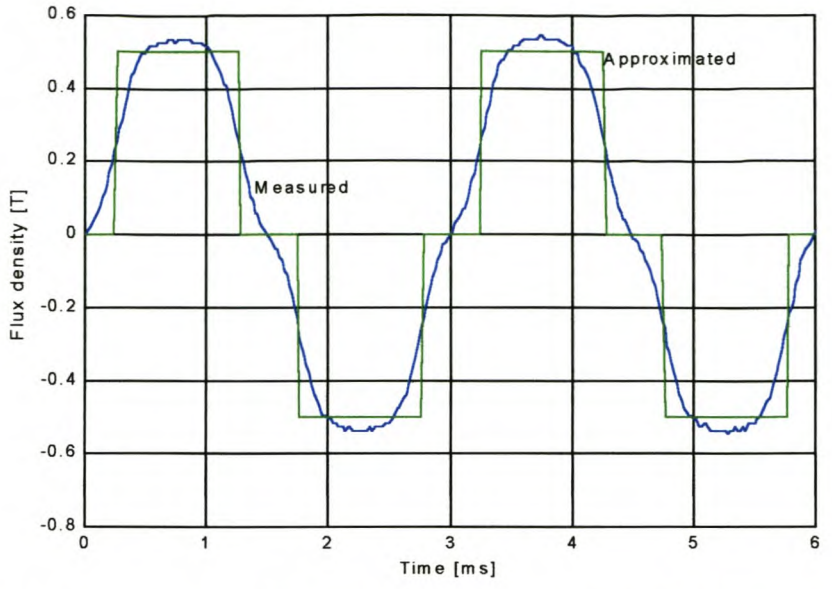

Figure 5.3: Measured and approximated airgap flux density waveforms of the AFPM machine.

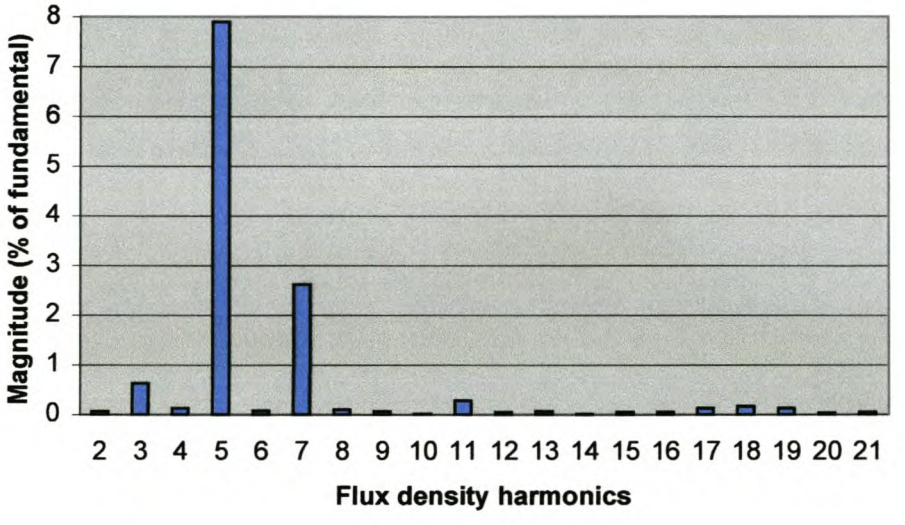

Figure 5.4: Harmonic content of the measured airgap flux density waveform

The computed fundamental amplitude was 0,559 T. It can be seen from Figure 5.4 that the 5th and 7th harmonics are quite significant and will result in underestimated eddy current losses if disregarded as in equation (2.55). This equation should rather be re-written to give the sum of the eddy current losses at each harmonic of the flux density as

$$P_e = \sum_i^N \frac{\pi\, B_{gi}{}^2\, \omega_i{}^2\, r_{con}{}^4\, n_{cp}\, m\, p\, N_c\, \Delta l}{8\, \rho_{cu}}, \qquad (5.3)$$

Stellenbosch University http://scholar.sun.ac.za

where $i = 1, 2, 3, \ldots, N$ are the harmonics and N the number of harmonics considered. The recalculated eddy current losses using equation (5.3) for the AFPM machine are 1,7 times higher than when only the fundamental component is considered. This suggests that a more accurate way to approximate the airgap flux density is needed, in order to calculate a more representative value of the eddy current losses by means of equation (5.3).

5.1.2 Gauss meter measurements of average airgap flux density

Measurements were done of the flux densities in the middle of the two airgaps of the AFPM machine by means of a digital Gauss meter. The results are shown in Figure 5.5. Flux 1 and Flux 2 are the flux density values measured in the two airgaps respectively.

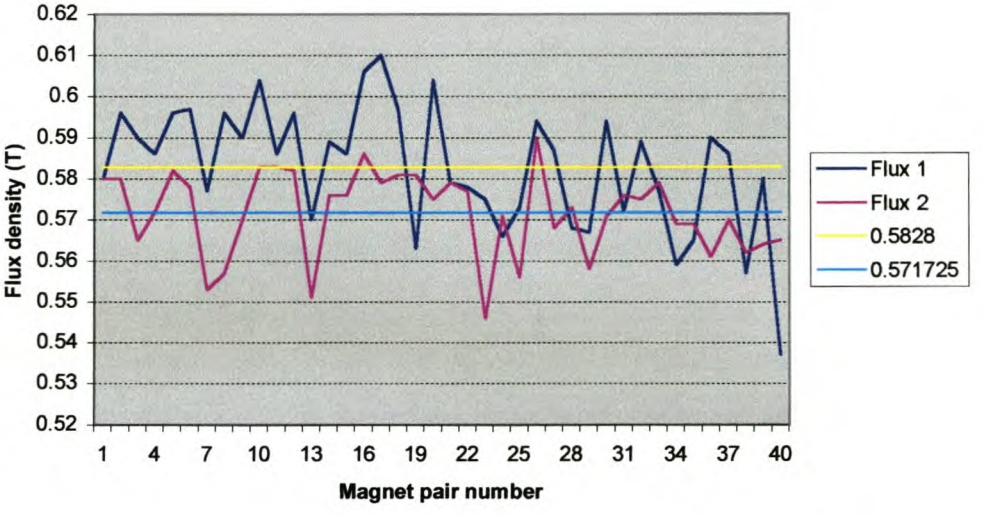

Figure 5.5: Measured peak airgap flux density between the magnet pairs.

It can be seen that the peak flux density varies from pole pair to pole pair. The averages of the peak flux densities of the two airgaps differ by about 1,7 %. This could be as a result of the difference in magnet thickness and the uneven sticking of the magnets on the rotor discs, and also the difference in the average of the two airgap-lengths (see Figure 4.14). The two average peak flux densities compares well with the peak flux density obtained from measurements in the previous section, which is 0,559 T.

Stellenbosch University http://scholar.sun.ac.za

5.1.3 EMF waveforms and harmonics

According to design predictions, the EMF waveforms should be approximately sinusoidal with a negligible harmonic content. To measure the the EMFs of the AFPM machine, the machine was operated at 1000 r/min and, first of all, the induced phase voltages of the two stators were measured. It was also found necessary to measure the EMFs of the four parallel phase coil conductors, since differences in the EMFs will cause large circulating currents. The EMF waveforms measured on the two stators are shown in Figure 5.6. The scale used on the vertical axis is 100 V/division and 1 ms/division on the horizontal axis.

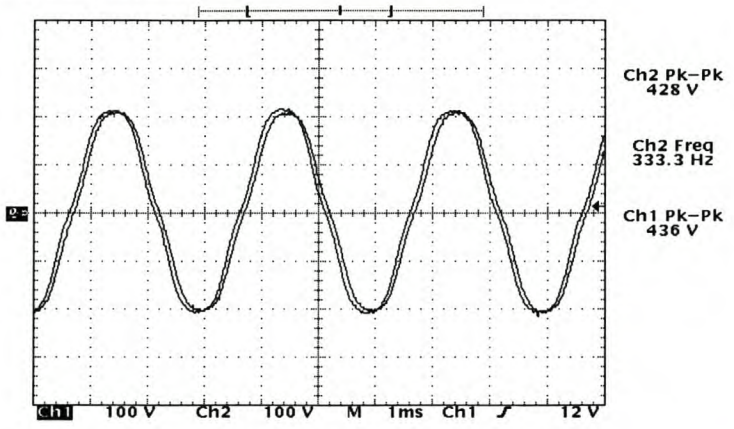

Figure 5.6: Measured phase voltages of the two stator stacks of the generator

From Figure 5.6, one notices that the voltages differ in amplitude by about 1% and also that they are displaced in phase by about 8,8 degrees. Thus, it is impossible to connect them in parallel as this will cause huge circulating currents. These differences in the stack voltages are attributed to (i) the imperfect construction of the machine stator in terms of the exact positioning of the stator coils on the stator bore and (ii) the differences in the airgap flux densities. The harmonic content of the two voltages are shown in Figures 5.7 and 5.8. The RMS values of the fundamental components of the voltages of the two stator stacks are 152 V and 150 V respectively.

Stellenbosch University http://scholar.sun.ac.za

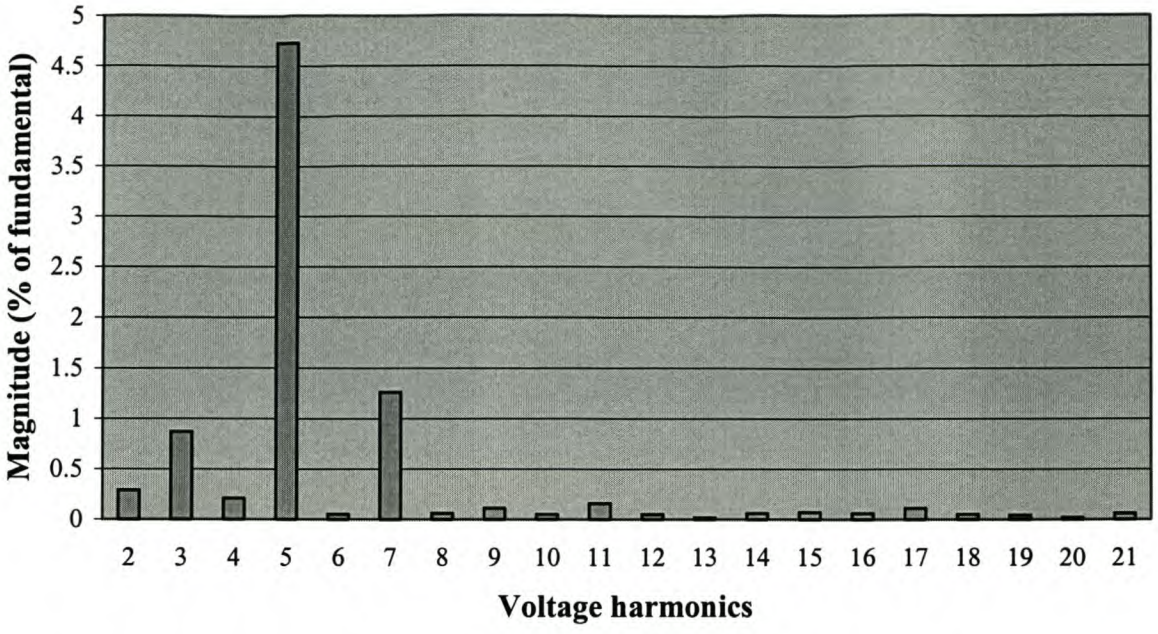

Figure 5.7: Harmonic content of a phase coil voltage of stator stack 1.

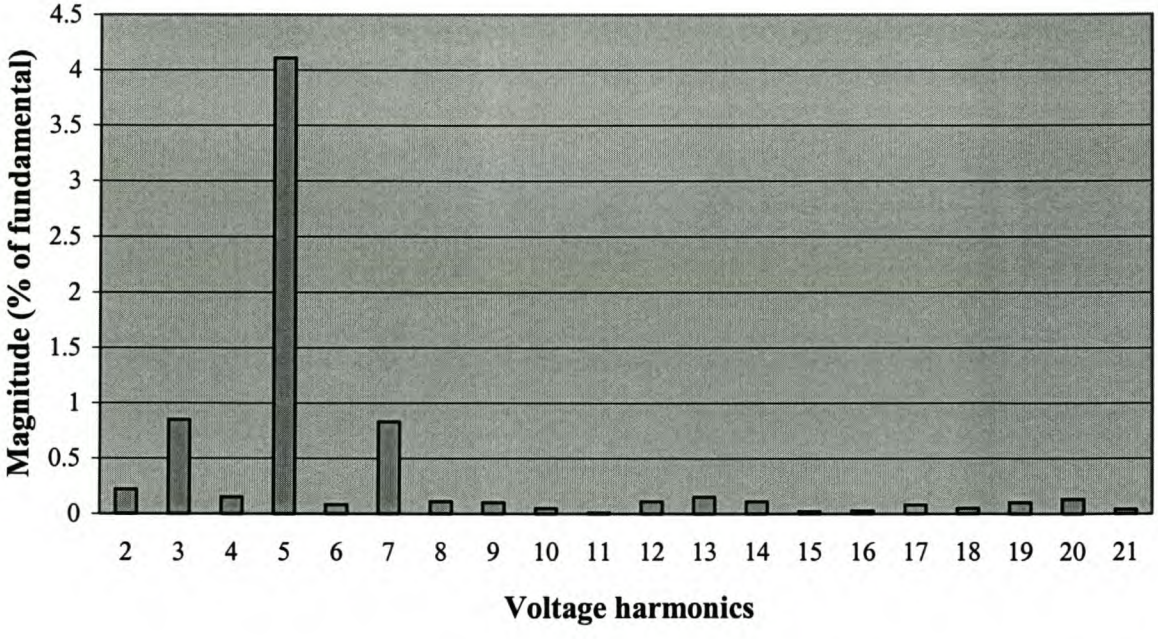

Figure 5.8: Harmonic content of a phase coil voltage of stator stack 2

The different phase coil conductor voltages were also measured with the parallel phase coil conductors open circuited. The measured results of the different phase coil conductor voltages (E_{1N}, E_{2N}, E_{3N} and E_{4N}) and their phase displacements relative to

Stellenbosch University http://scholar.sun.ac.za

the first conductor are tabulated in Table 5.1. It was found from measurements that the voltages induced in each of the four phase coil conductors differ in magnitude and also in phase. These differences will cause huge circulating currents in the phase coil as will be shown in section 5.1.3. The measured voltage waveform of one of the four parallel phase coil conductors is shown in Figure 5.9.

Table 5.1: Measured voltages and phase displacements in the 4 wires of a coil.

	Voltage	Phase displacement
E_{1N}	147 V_{RMS}	0°
E_{2N}	146 V_{RMS}	0,108°
E_{3N}	149 V_{RMS}	1,93°
E_{4N}	150 V_{RMS}	1,86°

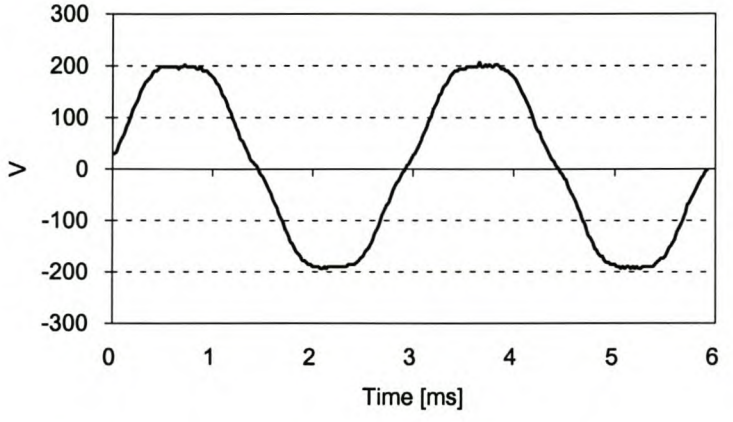

Figure 5.9: Measured open circuit voltage of one phase coil conductor.

5.1.3 Circulating currents in the parallel coil conductors.

The circulating currents in the parallel coil conductors, with the parallel coil conductors connected together are measured by means of a current sensor and oscilloscope. The parallel phase coil conductor currents, measured with the machine running at 590 r/min, are shown in Figure 5.10. Since the rated current of each parallel phase coil conductor is 2 A RMS, and since the circulating currents increase with the machine speed, it was not possible to increase the machine speed beyond 590 r/min.

Stellenbosch University http://scholar.sun.ac.za

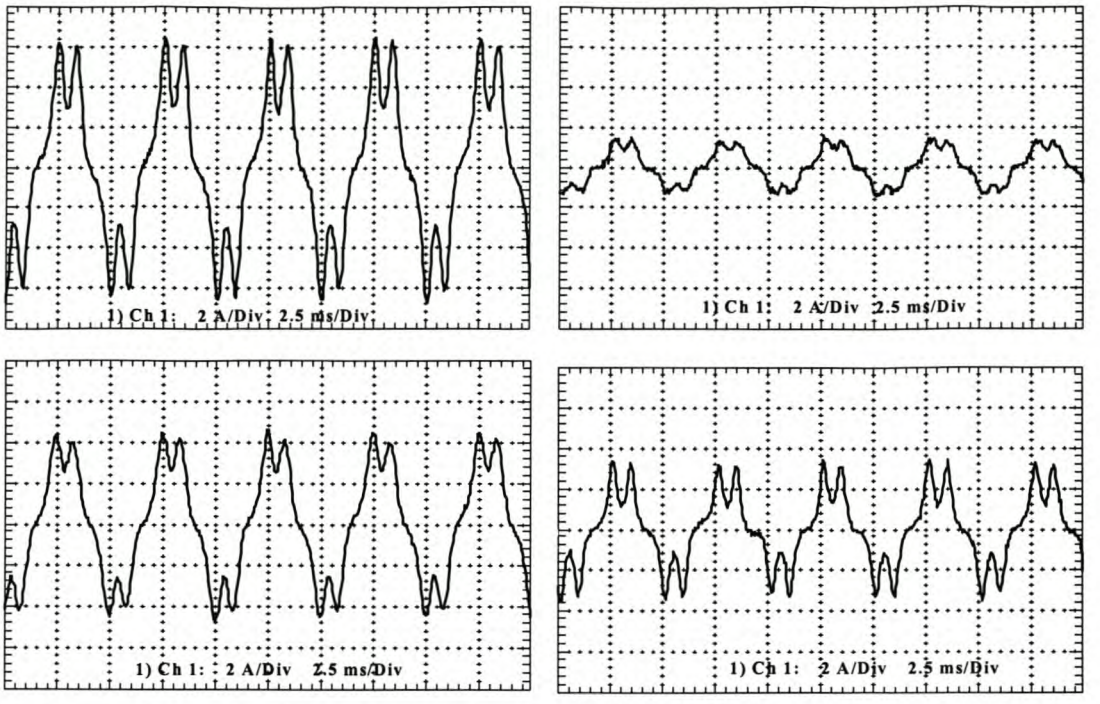

Figure 5.10: Circulating current in the four parallel phase coil conductors.

The RMS values of the measured circulating currents shown in Figure 5.10 are 3,66 A, 0,912 A, 2,72 A and 1,87 A respectively. It can be seen that the circulating currents in two of the phase coil conductors are already exceeding the 2 A RMS rating. This was one of the problems that made it impossible to test the machine's performance at rated speed and output power. The possible solutions to the circulating current problem are (i) to rectify the voltage of each parallel phase coil conductor, or (ii) to construct a new stator winding consisting of Litz - or stranded wire.

5.1.4 No-load thermal measurements

Thermal tests are done on the stator winding, with all the parallel phase coil conductors open circuited, to investigate the temperature rise due to the eddy current losses. The machine was run at different speeds for an extended period at each speed. Thereafter the temperature was noted. The stator temperature was measured by means of thermal sensors embedded in the stator coils. Figure 5.11 shows a plot of the measured temperatures versus the speed of the AFPM machine. It is clear that the eddy current losses significantly increase the temperature of the stator winding. Some measures should thus be taken to reduce these losses.

Stellenbosch University http://scholar.sun.ac.za

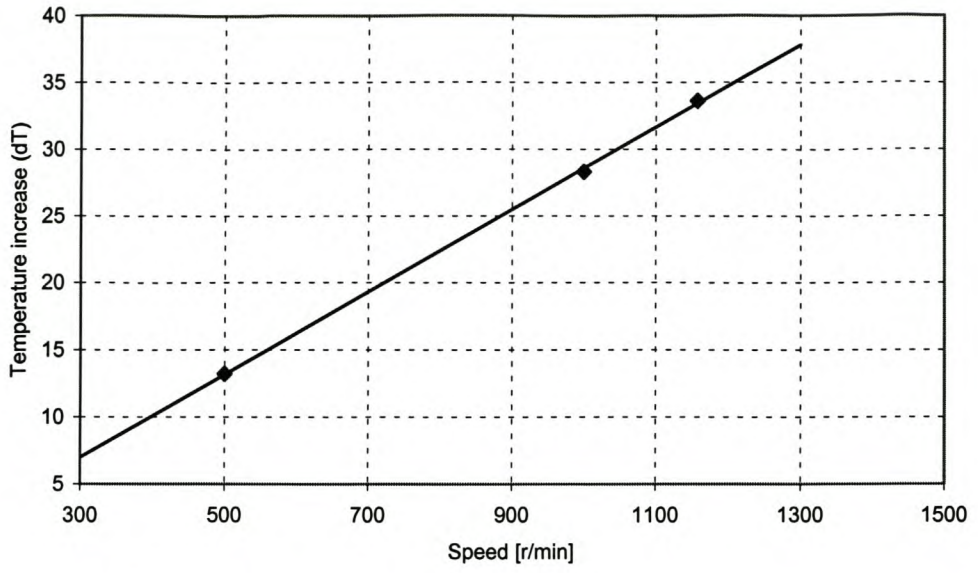

Figure 5.11: Plot of the no-load temperature increase versus machine speed.

Attempts to measure the temperature at higher speeds than 1100 r/min were unsuccessful. Some of the rotor magnets got loose and cut one stator stack's epoxy as shown in Figures 5.12 and 5.13. This suggests that another preventative measure should be put in place to ensure that the magnets don't get loose due to the centrifugal forces. To achieve this, it was decided to drill holes in the magnets and also partially into the rotor discs in order to pat pins in the holes to hold the magnets at their desired positions (see Figure 5.14). The machine was then assembled again and tests were conducted to determine whether rectifying the voltages of each of the four parallel phase coil conductors would solve the circulating current problem. This also opened up the possibility of testing the machine at higher speeds.

Stellenbosch University http://scholar.sun.ac.za

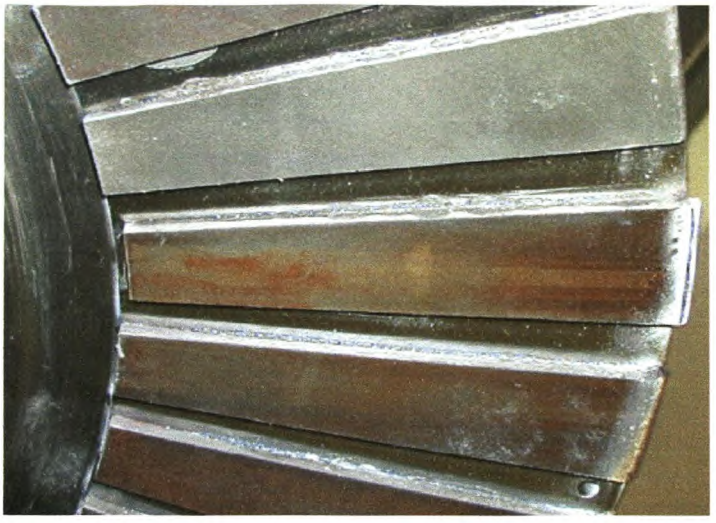

Figure 5.12: Rotor magnet that got loose at a speed of 1100 rpm.

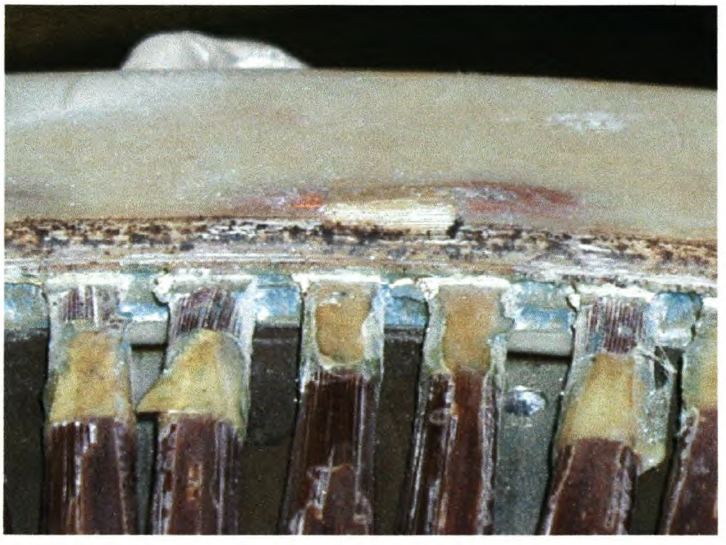

Figure 5.13: Stator cut-out due to loose rotor magnet.

Figure 5.14: Rotor magnets with pins inserted.

Stellenbosch University http://scholar.sun.ac.za

5.2 Rectifier tests

Load tests are conducted by connecting 3-phase rectifiers to the output of each of the open circuited four parallel phase coil conductors of three phase coils of one stage of the machine. The resulting rectifier DC outputs of each rectifier are connected in parallel to give a single DC output. The DC output was connected to a filter and resistive load as shown in Figure 5.15. The no-load rectification test was successful since there were no circulating currents in the parallel phase coil conductors.

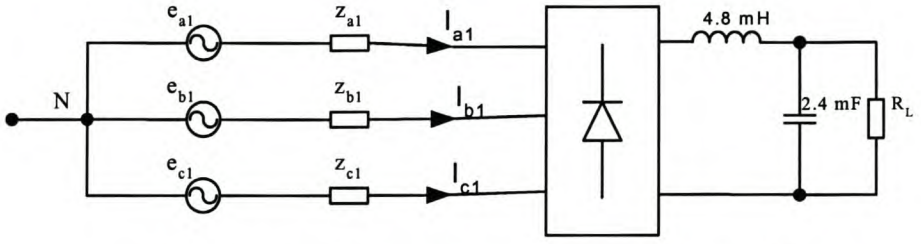

Figure 5.15: Circuit diagram of connected rectifier.

Simulations, and measurements on a single stage prototype AFPM generator described in Appendix C, showed that it is best to connect an inductor in series with the capacitor and the load as shown in Figure 5.15. It was found that this leads to an increase in power output and a reduction in the harmonics imposed to the machine by the rectifier. The measured RMS voltages and currents in Table 5.2 represent the average values of the measurements of the four parallel phase coil conductors. The measurements in Case 1 had no series filter inductance connected to the rectifiers, while in Case 2, a 4,8 mH inductance was connected to the rectifiers. It can be seen that the measured results obtained for the two cases compares very well with each other, but once again it is observed that the output power in Case 2 is higher than in Case 1.

Stellenbosch University http://scholar.sun.ac.za

Table 5.2 Measured results of rectifier connected to the machine.

Parameter	Case 1	Case2
Inductance at output [mH]	0	2,4
RMS phase voltage [V]	139	141
RMS conductor current [A]	2,48	2,44
No-load DC voltage [V]	380	379
DC link voltage [V]	313	311
DC current [A]	10,6	11,6
Frequency [Hz]	334	333
Output power [kW]	3,318	3,608
Voltage regulation [%]	4,3	4,1

Other measurements are also done to determine the wave shapes and magnitudes of the full-load currents in each of the parallel phase coil conductors, with no inductor connected (Case 1) and the other with an inductor connected to the circuit (Case 2). The currents in each of the four parallel phase coil conductors are shown in Figures 5.16 and 5.17 for Case 1 and 2 respectively. The RMS values of the measured parallel phase coil conductor currents in Figure 5.16 are 2,1 A, 2,0 A, 2,2 A and 2,08 A respectively and those in Figure 5.17 are 2,1 A, 1,97 A, 2,26 A and 2,08 A respectively. The measured currents in Figure 5.17 are looking better than those in Figure 5.16 as expected, because of the series inductor. Furthermore, it can be seen that the currents of Figures 5.16 and 5.17 divide equally between the parallel conductors. The use of the rectifiers is thus in this sense a solution to the circulating current problem, as mentioned earlier.

Stellenbosch University http://scholar.sun.ac.za

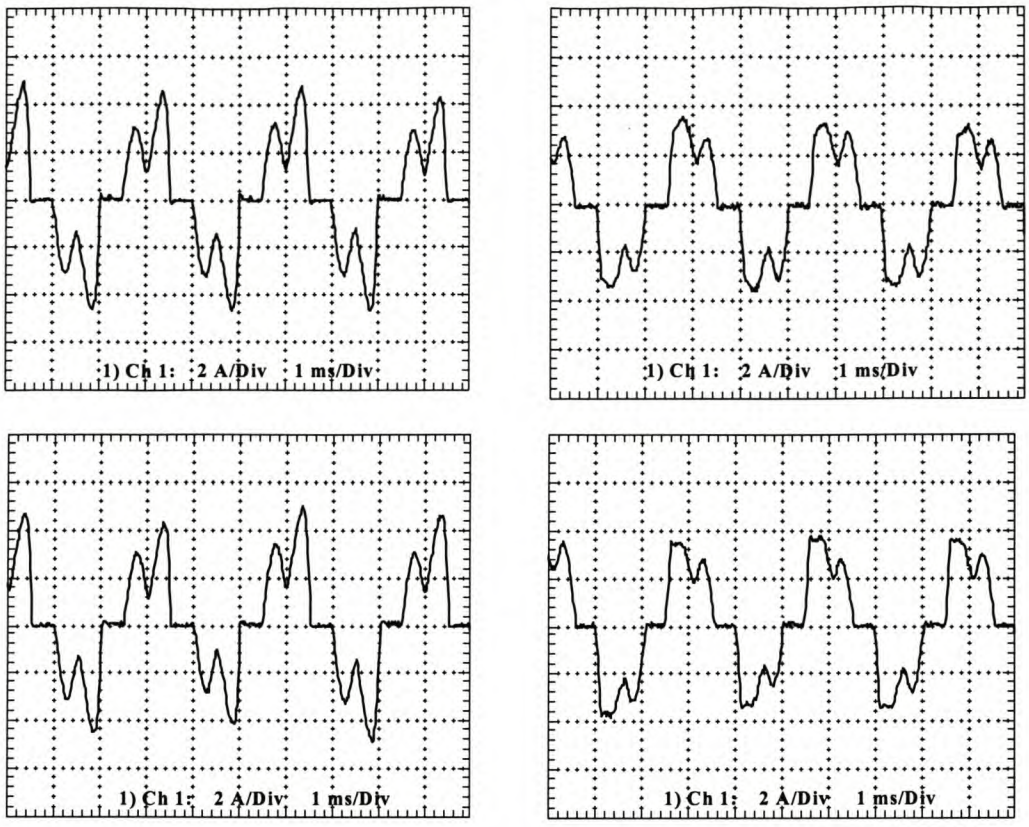

Figure 5.16: Phase A parallel coil conductor currents for Case 1 (no DC inductor).

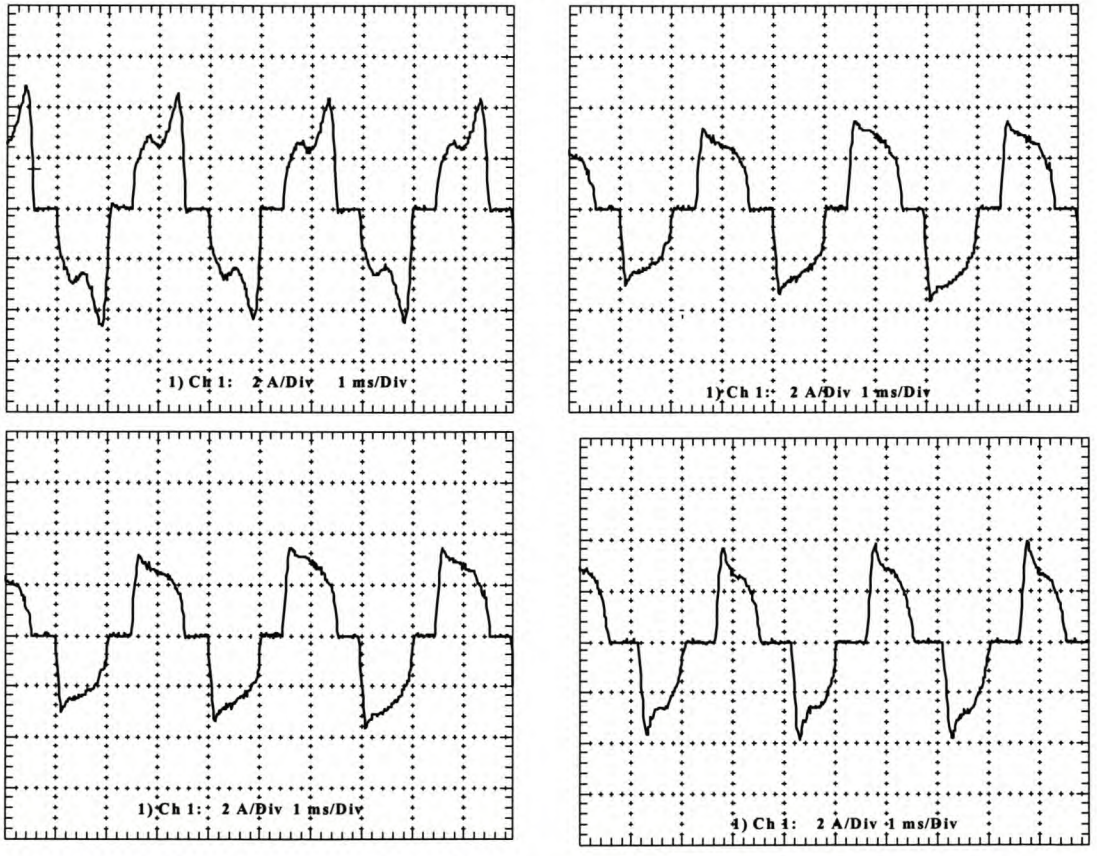

Figure 5.17: Phase A parallel coil conductor currents for Case 2 (with DC filter inductor).

Stellenbosch University http://scholar.sun.ac.za

5.3 Stranded parallel conductors tests

Another solution investigated to solve the circulating current problem was by constructing a new stator consisting of coils with twisted parallel conductors. For experimental purposes, three differently twisted (stranded) coils were wound, one slightly stranded, one medium stranded and another one highly stranded as shown in Figure 5.18.

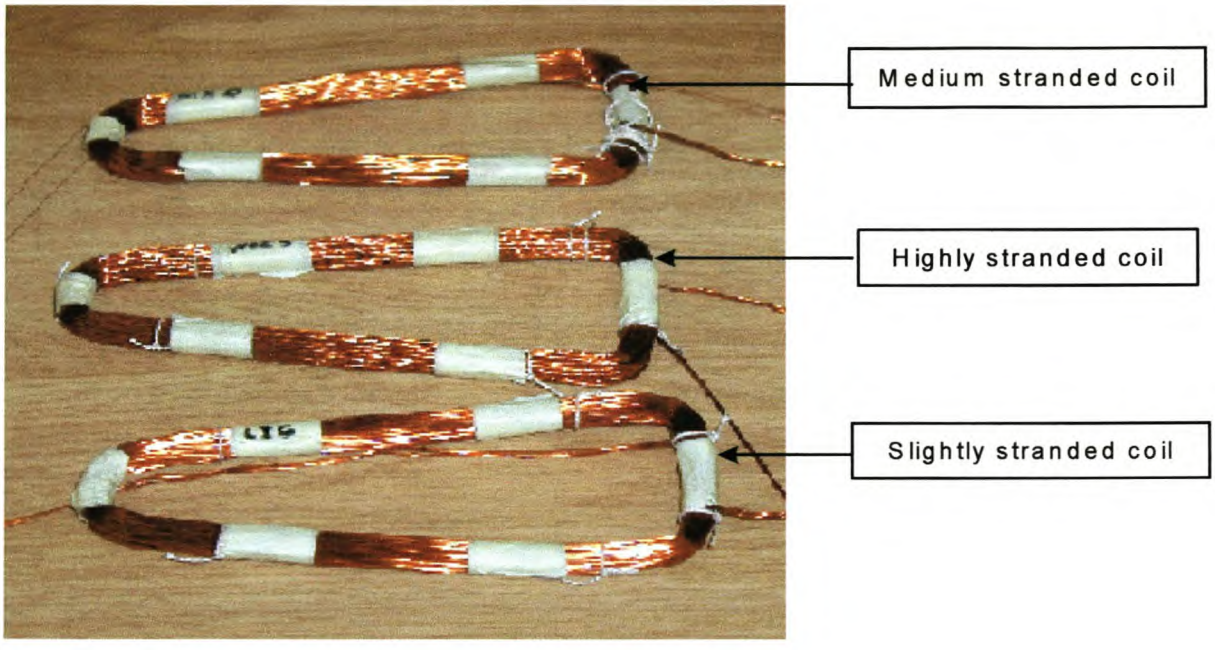

Figure 5.18: Stranded coils used in the measurement of circulating currents.

It was found that by just slightly twisting the parallel conductors a better filling factor is obtained than with the conductors highly stranded. The question investigated is to what extend the circulating currents are reduced by twisting the parallel conductors. Figures 5.19, 5.20 and 5.21 show the measured circulating currents of each of the three cases investigated, i.e. slightly, medium and highly stranded coils respectively. The measurements were done with the machine running at a speed of 1000 r/min. The RMS values of the measured currents of the slightly stranded coil conductors are 52 mA, 40 mA, 90 mA and 110 mA respectively. It is clear that using stranded wires drastically reduces the circulating currents in the parallel coil conductors.

Stellenbosch University http://scholar.sun.ac.za

The RMS values of the currents measured in the four parallel conductors of the medium stranded coil are 42 mA, 24 mA, 43 mA and 58 mA respectively. Thus, there is a reduction in the maximum value of the circulating currents in the medium stranded coil. The RMS values of the circulating currents measured in the parallel conductors of the highly stranded coil conductors are 9,34 mA, 12,5 mA, 10,6 mA and 7,1 mA respectively.

It can thus be concluded that by using stranded coil conductors the circulating currents are drastically reduced. Stranding parallel conductors is also a more cost effective way than using Litz wire. It is also beneficial for the AFPM generator, since the number of diodes needed for the rectification of the different phase coil voltages are reduced from 480 to 120 per stage (75 % reduction).

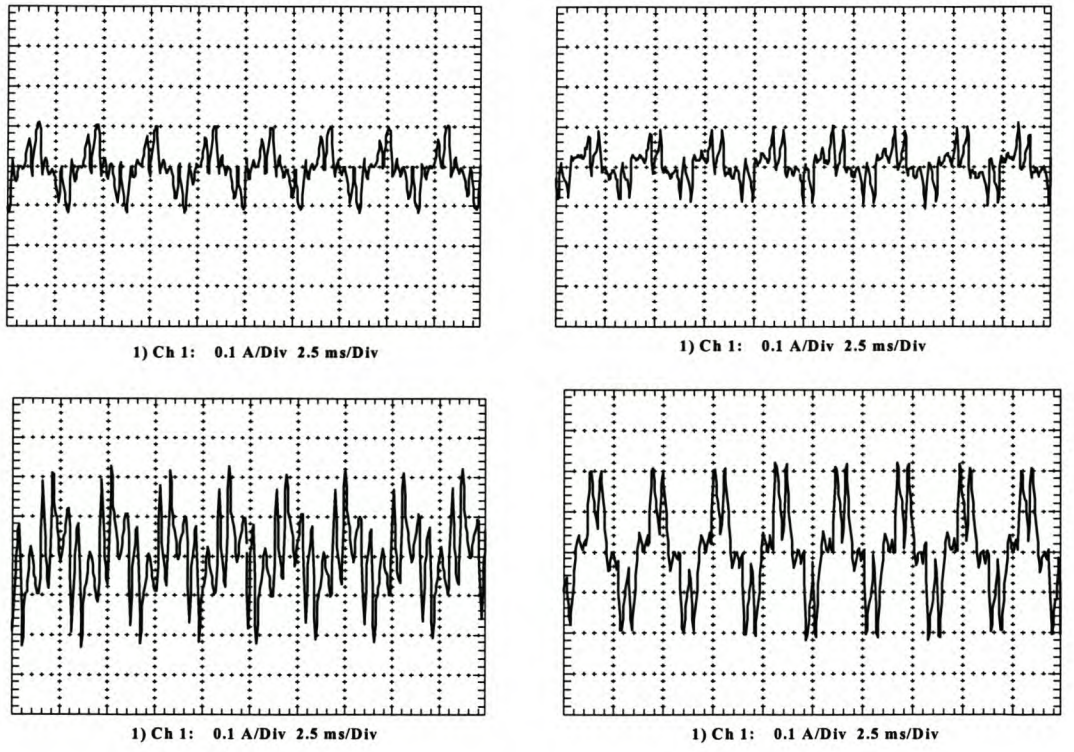

Figure 5.19: Circulating currents of the slightly stranded coil.

Stellenbosch University http://scholar.sun.ac.za

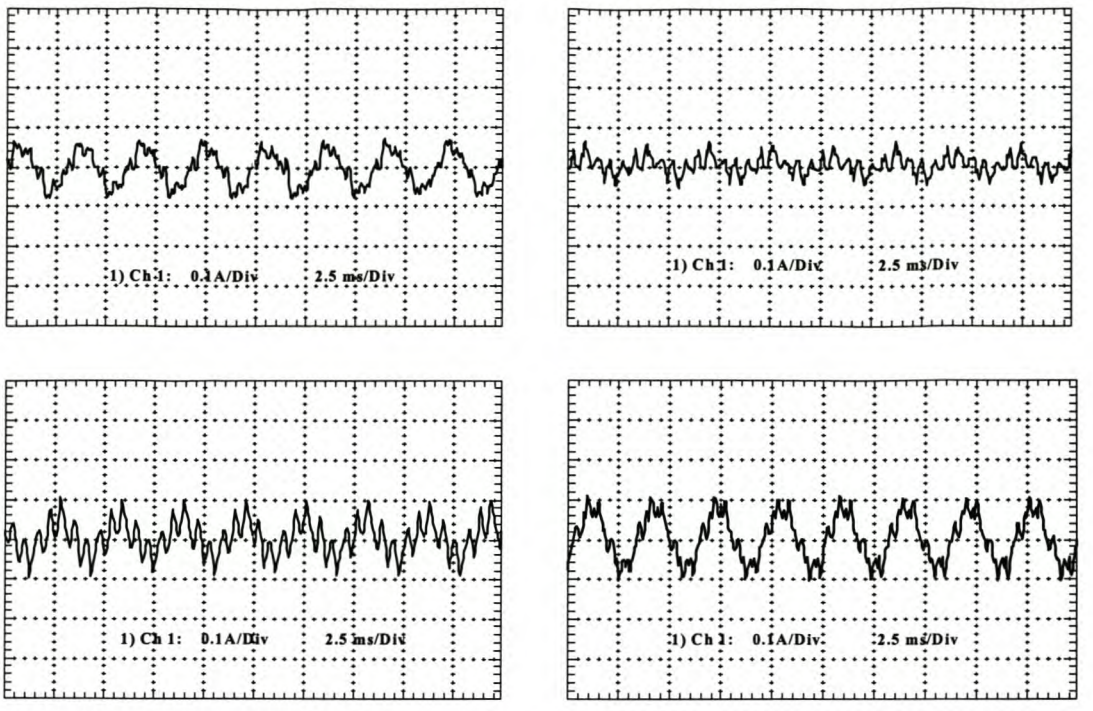

Figure 5.20: Circulating currents of the medium stranded coil.

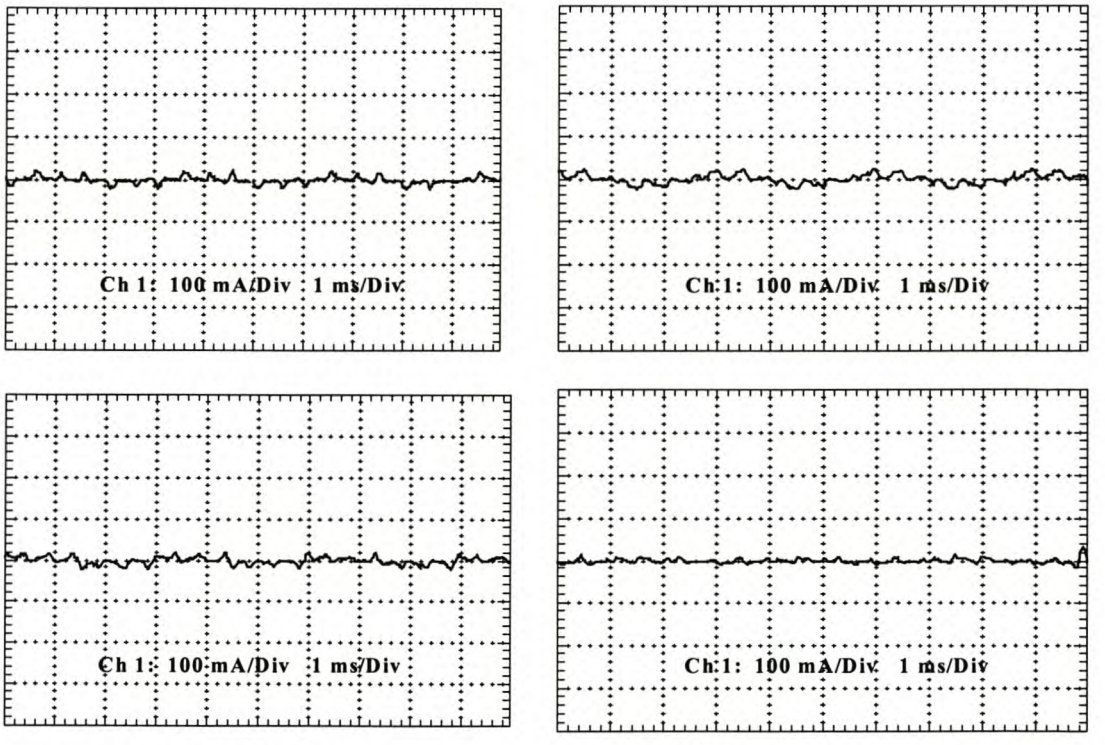

Figure 5.21: Circulating currents of the highly stranded coil.

Stellenbosch University http://scholar.sun.ac.za

6. CONCLUSIONS AND RECOMMENDATIONS

This chapter gives an overview of the work described in this thesis (section 6.1), it come to the most important conclusions in section 6.2 and finally give some recommendations for future work in section 6.3.

6.1 Overview

The design, construction and analysis of a double stage, 300 kW generator is described. The magnetic and electrical design equations are derived for sinewave and BDC (squarewave) operations of the AFPM machines. The thermal design approach taken is also described. The machine is optimised for maximum torque per current loading. A Matlab program code is developed to do the calculations needed in the optimisation and the calculation of the machine parameters.

FEM simulations are conducted to investigate the severity of the PM magnetic attraction force between the rotor discs. It is found that the yoke thickness, obtained from the electrical design, had to be increased in order to increase its mechanical strength. The construction of the rotor and stator is also described. Measurements are conducted to evaluate the machine electrically and thermally.

The no-load measurements conducted on the 300 kW machine showed that the circulating currents in the parallel wires of the stator winding were underestimated. It is showed that the induced voltages in each of the four conductors of a coil are different in magnitude and phase, which resulted in huge circulating currents. Some of the possible solutions investigated are either rectifying each conductor from a coil, or using a coil consisting of stranded conductors. Both solutions worked very well in eliminating the circulating currents at no load. It was also found that it is not necessary to use highly stranded coils, because by even stranding the coil conductors slightly causes a dramatic reduction in the circulating currents.

Stellenbosch University http://scholar.sun.ac.za

6.2 Conclusions

The most important concluding remarks reached from this research are as follows:

- The equations for the electrical design of a double stage AFPM that leads to the electrical design optimisation are given. It is found that the sinewave AFPM machine has a very low mass due to the higher pole number compared to the BDC machine. The sinewave machine looks favourable, but does not necessarily satisfy the mechanical strength requirement.
- FEM simulations conducted showed that the thickness of the yoke had to be doubled from 6 mm, in order to allow a maximum deflection of less than 0,34 mm on the rotor discs due to the magnetic attraction forces. This resulted in an undesirable decrease in the output power to active mass ratio of about 34 %.
- The calculation of the eddy current losses of the 300 kW AFPM machine, by means of the empirical formula, was not accurate. It is found that a more accurate way to determine the eddy current losses is by taking into account all the flux density waveform harmonics in the calculation thereof.
- It is found necessary to measure the eddy current losses in the machine in order to verify the formula used in the design of the machine. This measurement was difficult because there was no torque sensor available to measure the shaft input power.
- The circulating currents in the parallel phase coil conductors could be eliminated by rectifying each individual coil conductor or by using stranded coil conductors or Litz wires. The stranded coil conductor solution is found to be a more cost effective solution compared to the other options considered.

6.3 Recommendations

Future research work is necessary on the overall AFPM machine design optimisation consisting of a combination of electrical, mechanical and thermal designs, possibly by means of a FEM simulation package.

Stellenbosch University http://scholar.sun.ac.za

It is believed that if the following recommendations are taken into account during the machine design and construction, it could serve as improvement in the behavioural characteristics of the AFPM machine.

6.2.1 Rotor structure

The following should be considered for the structural improvement of the rotor:

- Due to the fact that the magnets could not withstand the centrifugal forces at speeds higher than 1150 r/min, the following solutions should be implemented:
  - Totally or partially embedding the magnets in the rotor disc surface.
  - Fastening a non-magnetic (aluminium) rim on the outside of the rotor magnet diameter.
- Finding another material preferably cheaper and lighter than steel to use for the middle disc of the double stage machine and able to withstanding the magnetic attraction forces between the rotor discs.
- Construct a single stage rather than a double stage AFPM machine.

6.2.2 Stator structure

The following improvements on the stator construction could be considered:

- Increasing the mechanical clearance between stator and rotor to 2 mm each side. This will also improve ventilation of the machine because of the resulting increase in machine airgap volume.
- When reducing the eddy current losses in the stator winding by using thinner parallel copper conductors, one should try to eliminate the resulting circulating currents in the parallel coil conductors. This can be achieved by considering the following options:
  - Using Litz wire consisting of twisted copper strands of a diameter less than the skin depth [9, pp 773-774]. This type of wire arrangement has a typical filling factor of 0,3 and is also more expensive than normal conductors.
  - Using slightly stranded parallel coil conductors, which is a more cost effective solution compared to Litz wire.

Stellenbosch University http://scholar.sun.ac.za

- When using parallel coils, ensure that (i) all the coils are similar and (ii) that the spatial positioning of the coils on the stator bore should be made very accurate.

6.2.3 Machine housing

The casing and support of the entire stator and rotor should be designed carefully in order to avoid addition of unnecessary mass to the rest of the machine. One way of achieving this is by mounting the stator of the AFPM machine on the heat engine's stationary frame and the rotor on its axis.

Stellenbosch University http://scholar.sun.ac.za

REFERENCES

[1] E. R. Laithwaite, "A History of Linear Electric Motors," *Macmillan Education Ltd., London, **1987**.*

[2] C. C. Chan, "Axial-field Electrical Machines – Design and Applications," *IEEE Trans. on Energy Conv., Vol. EC-2, No. 2, pp. 294-300, June **1987**.*

[3] W. S. Leung, J. C. C. Chan, "A New Design Approach for Axial-field Electrical Machines," *IEEE Trans. on PAS, Vol. PAS-99, No. 4, pp. 1679-1685, July/Aug. **1980**.*

[4] P. Campbell, D. J. Rosenberg, D. P. Stanton, "The Computer Design and Optimisation of Axial-field Permanent Magnet Motors," *IEEE Trans. on PAS, Vol. PAS-100, No. 4, pp. 1490-1497, April **1981**.*

[5] E. Spooner and B. J. Chalmers, "Toroidally-Wound, Slotless, Axial-flux, PM, Brushless DC Motors," *Proceedings of Int. Conf. Electrical Machines, vol. III, pp. 81-86, **1988**.*

[6] E. Spooner, A. C. Williams, "Direct Coupled, Permanent Magnet Generators for Wind Turbine Applications," *IEE Proc.-Electr. Power Appl., Vol. 143, No. 1, pp. 1-8, Jan **1996**.*

[7] P. Campbell, "Performance of a Permanent Magnet DC Machine," *IEE Journal on Electric Power Applications, Vol. 2, No. 4, pp. 139-144, Aug. **1979**.*

[8] P. Campbell, "Principles of a Permanent Magnet Axial-Field DC Machine," *Proc. of IEE, Vol. 121, No. 12, pp.1489-1494, Dec 1974.*

[9] N. Mohan, T. N. Underland, W. P. Robbins, "Power Electronics: Converters, Applications and Design," 2nd Edition, *John Wiley & Sons, Inc., New York, **1995**.*

[10] F. Caricchi, F. Crescimbini, F. Mezzetti and E. Santini, "Multi-stage axial-flux PM Machine for Wheel Direct Drive," *IEEE Trans. on Ind. Appl., vol. 32, pp. 882-888, July/Aug. **1996**.*

[11] F. Caricchi, F. Crescimbini, O. Honorati, G. Lo Bianco and E. Santini, "Performance of a Coreless-winding Axial-flux Permanent Magnet Generator

Stellenbosch University http://scholar.sun.ac.za

with Power Output at 400 Hz, 3000 r/min," *IEEE Tans. Ind. Applicat., vol. 34, pp. 1263-1269, Nov./Dec.* ***1998***.

[12] N. F. Lombard, " Design and Evaluation of an Iron-less Stator Axial-flux Permanent Magnet Machine," *M. Sc. (Eng.) thesis, University of Stellenbosch,* ***1997***.

[13] N. F. Lombard and M. J. Kamper, " Analysis and Performance of an Iron-less Stator Axial-flux PM Machine," *IEEE Trans.on Energy Conversion, Vol. 14, No. 4, pp. 1051-1056, Dec.* ***1999***.

[14] G. W. Carter, "The Electromagnetic Field in its Engineering Aspects, " Longmans, 2nd ed, pp. 254, ***1967***.

[15] J. R. Hendershot Jr, T. J. E. Miller, "Design of Brushless Permanent-magnet Motors," *Magna Physics Publishing, OH and Oxford University Press, NY,* ***1994***.

[16] J. F. Gieras and M. Wing, "Permanent Magnet Motor Technology, Design and Applications," *Marcel Dekker, Inc. New York,* ***1997***.

[17] R. Wang, R. T. Dobson and M. J. Kamper, "Thermofluid analysis of an Axial Flux Permanent Magnet (AFPM) generator, " *R & D Journal, Vol. 17, No. 1, pp. 18-26, March* ***2001***.

[18] W. F. Ray, "The Effect of Supply Reactance on Regulation and Power Factor for an Uncontrolled 3-Phase Bridge Rectifier with a Capacitive Load," *IEE Conf. Publication, No. 234, pp. 111-114, 1984.*

Stellenbosch University http://scholar.sun.ac.za

A. DESIGN PROGRAM CODE LISTING

This appendix gives the Matlab program code listing used in the optimisation of the AFPM machines, by calculating the different machine parameters form the equations derived in Chapter 2. The first part deals with the sinewave AFPM machine design and the second part with the design of BDC (squarewave) machine.

A1 Sinewave AFPM machine design code listing

```
%********** Design of 2-Stage, axial flux, PM machine *****
%**********With sinusoidal flux distribution and parallel operation
%********** Keeping yh constant ****************************
%*********** Last updated: 7 July 2000 at 17:00 **********
clear all;
format long;
clc;
%************ Define Constants. ************
Rshft = 0.035;                    % Induction machine shaft diameter
m = 3;                            % number of phases
q = 1;                            % number of coils/pole/phase
kf = 0.5 ;                        % filling factor
Ks = 1;                           % distribution factor
dcu = 0.008;                      % copper diameter 8 mm
Bg = 0.5;                         % air-gap flux density
n = 2300;                         % speed in rpm
%n = input('Please enter the shaft speed in [rpm]? n = ');
Bgy = 0.4;                        % ratio of Bg/By
hm = 0.005;                       % magnet length of 7.5 mm
lg = 0.01;                        % airgap length of 10 mm
%yh = 0.012;                      % select yoke of 12 mm thickness
yhm = 0.008;                      % mid yoke thickness [8 mm]
VR = 7.5;                         % voltage regulation
DPF = 0.9549;                     % Displacement power factor
Vd = 750;                         % DC link voltage
```

Stellenbosch University http://scholar.sun.ac.za

```
%Vd = input('Please enter the desired DC rectifier voltage? Vd = ');
Erms = 0.48*Vd;                    % RMS Voltage of Machine (57.1)
Stg = 2;

%********* Torque and phase current ***********************
Pd = 322e3;                        % power output of rectifier 322 kW
%Pd = input('Please enter the desired rectifier power output in kW? Pd = ')*1000;
Id = Pd/(Vd);                      % Rectifier output current [A]
Irms1 = 0.8*Id;                    % RMS armature phase current (57.2)
Irmsd = Irms1/(DPF); RMS phase current [A] (53.3)
Vt = Pd/(sqrt(3)*Irmsd*0.96);%Line to line voltage of AFPMM
Irms = Irmsd/2;                    % RMS current per stage [A]
Pg = sqrt(3)*Vt*Irms;% Power at generator terminals

%************** Determine J, Nph, dL and ri **************
************************************************************
M = 1000;                          % number of data points
ro = input('Please enter the outer radius in [m]? ro = ');
dL = linspace(2*lg,ro/2,M);        % delta L
ri = ro-dL;                        % inner radius
re = (ro+ri)/2;                    % average radius
re1 = sqrt(ro^2+ri.^2)/sqrt(2);    %mass middle point of magnet
Kr = ri/ro;
Qse = pi*(ri-lg)./(3*re);          % distribution angle
Ksk = 2*sin(Qse/2)./Qse;           % skew factor

%********* Calculating J, Nph vs ri and dL ****************
Nph = fix(15*Erms./(sqrt(6)*n*Ksk*Ks* Bg.*dL.*re));     % number serie turns per
phase
Jrms=m*Irms*Nph./(kf*dcu*pi*(ri-lg));%current density [A/m^2]

%********** Calculations of Pmax, Ns ***************
Pmax = 2*pi*(ri)/(m*lg);      % number of poles
pmx = fix(Pmax);                        % round down all pole numbers
```

Stellenbosch University http://scholar.sun.ac.za

```
kk = mod(pmx,2);

for i=1:length(Pmax),          % get rid of odd numbered poles
        if kk(i) == 0,
  P(i) = pmx(i);                          % keep even pole numbers
        else
  P(i) = pmx(i)-1;                % reduce odd pole numbers by one
        end
end

a = Pmax/2;                     % number of parallel paths
f = n*Pmax/120;                 % frequency [Hz]
Ns = (2*a.*Nph./(Pmax*q));% number of turns per coil
Acon = Irms./(a.*Jrms);         % conductor area
Acus = Ns.*Acon/kf;             % coil copper area
Acon1 = kf*Acus./Ns;            % area of conductor [m^2]
Ncp = input('Enter the number of parallel wires per coil? Ncp = ');
Dwire=sqrt(4*Acon/pi)/sqrt(Ncp); % conductor diameter [m]

%*********Copper losses Pcu and Rph ******************
le = (pi*(ro+ri)./Pmax)+2*lg;% length of windings [D,29.1]
tc = 75;                        % conductor temperature
Yt = 0.0039;
P20 = 17e-9;
Pt = P20*(1+Yt*(tc-20));% temperature constant
Rph = 2*m*Nph.^2*Pt.*(dL+le)./(pi*kf*dcu*(ri-lg));% phase resistance [Ω]
Pcu = m*Irms.^2.*Rph;           % copper losses [W]
We = 2*pi*f;
Lwire = Ncp*m*Pmax.*dL.*Ns;     % length of wire [m]
Pe=pi*Bg^2*We^2.*(Dwire/2)^4.*Lwire/(8*Pt);%Eddy current loss
Pdev = Pg+Pcu+Pe;               % developed power [W]
Ws = 2*pi*n/60;                 % synchronous speed [rad/sec]
T = Pdev/Ws;                    % torque [N.m]
```

Stellenbosch University http://scholar.sun.ac.za

%*** Determining the Volumes and Active mass of AFPM *****

```
R = 7880;                          % density of copper kg/m^3
k = 2/3;
Qm = 4*pi./(3*P);                  % magnet angle [rad]
Qp = 2*pi./P;                      % pole pitch in rad
Volm = (re.*Qm.*dL*hm)*2.*P;       % magnet volume [m^3]
Volm1=P.*(ro^2-ri.^2).*Qm*hm;
yh = 2.2*Bgy*re./P;                % yoke thickness [m]
yh1=[0.007*ones(1,M)];
Ph=2.2*Bgy*re./yh;
Voly = pi*(ro^2-(ri-0.055).^2).*yh; % yoke volume [m^3]
Volw = m*kf*q*Acus.*(le+dL).*P;    % volume of windings [m^3]
Massy = Voly*R;                    % mass of yoke in [kg]
Massm = Volm*R;                    % mass of magnets in [kg]
Massw = R*Volw;                    % mass of windings [kg]
Myx = R*P.*(ro^2-ri.^2).*Qm*yx;% yx is extra yoke added
Midplate = R*P.*(ro^2–ri^2).*Qm*yhm/2;% mass of midplate [kg]
Masstots1 = Massm+2*Massy+Massw+Myx;% mass [kg]of 1 stage
Masstots = Massm+2*Massy+Massw;% activemass [kg] of 1 stage
Masstotd1 = 2*Massm+2*Massy+2*Massw+Midplate+2*Myx;% total mass for
double stage
Masstotd = 2*Massm+2*Massy+2*Massw;% active mass for double stage
V1 = pi*(ro^2-ri.^2)*lg;           % volume at dL
V2 = pi*(2*(hm+yx)+lg)*((ro+3*lg)^2-ro^2);% volume above ro
V3 = pi*(ri^2-(ri-3*lg)^2)*(2*(hm+yx)+lg);% volume below ri
Vcu = V1+V2+V3;                    % volume enclosing the copper

TpJ = T./Jrms;                     % torque in [N.m]
PpMass = Pg./Masstots;             %
Eff = 100*Pg./Pdev;                % efficiency [%]
```

% Determining the total mass of the AFPM

```
Midp = R*2.5*lg*pi*(ri^2-(ri-2.5*lg)^2);        %inactive middle plate mass
```

Stellenbosch University http://scholar.sun.ac.za

```
ly = (4*(hm+yx)+2*lg+yhm);                  % axial length of base
myoke=2*R*ly*pi.*(ri^2-0.143^2);            % inactive mass of yoke
msupport = R*ly*pi*((ri-2.5*lg)^2-Rshft^2); % supporting part
Massx= Midp+myoke+msupport;                 % total extra mass [kg]
Mass =Masstotd+Massx;

%*********************************************************
disp('***2-STAGES CONNECTED IN PARALLEL ***************');
disp('      OUTPUT RESULTS  (Sinusoidal Operation)');
disp(['.....Date:  ',datestr(now),'.....']);
disp('.....');
format short;
[Y,I] = max(TpJ);                           % determine the maximum T/J point
disp(['The optimum design result ri/ro=',num2str(ri(I)/ro), ' is:']);
disp(['Number of stages = ',num2str(Stg),'']);
disp(['Pout = ',num2str(Pd/2000),' kW per stage']);
disp(['Vd = ',num2str(Vd),' V']);
disp(['Erms = ',num2str(Erms),' V']);
disp(['Irms = ',num2str(Irms),' A per stage']);
disp(['Pdev = ',num2str(Pdev(I)/1000),' kW per stage']);
disp(['T = ',num2str(T(I)),' N.m per stage']);
disp(['n = ',num2str(n),' rpm']);
disp(['VR = ',num2str(VR),' %']);
disp(['ro = ',num2str(ro),' m']);
disp(['dL = ',num2str(dL(I)),' m']);
disp(['ri = ',num2str(ri(I)),' m']);
disp(['Nph = ',num2str(fix(Nph(I)))]);
disp(['Jrms = ',num2str(Jrms(I)/1e6),' A/mm^2']);
disp(['kf = ',num2str(kf),' filling factor']);
disp(['Poles = ',num2str(P(I))]);
disp(['a = ',num2str(fix(a(I)))]);
disp(['Pole pitch = ',num2str(Qp(I)),' rad']);
disp(['Magnet angle = ',num2str(Qm(I)),' rad']);
disp(['Qipg = ',num2str(2*pi/(3*P(I))),' rad']);
```

Stellenbosch University http://scholar.sun.ac.za

```
disp(['f = ',num2str((P(I)*n/120)),' Hz']);
disp(['Ns = ',num2str(fix(Ns(I))),' turns/coil']);
disp(['Awire = ',num2str(Acon(I)*1e6),' mm^2']);
disp(['Acus = ',num2str(Acus(I)*1e6),' mm^2']);
disp(['Number of parallel wires/coil=',num2str(Ncp),' ']);
disp(['Dwire = ',num2str(1e3*Dwire(I)),' mm']);
disp(['Pcu = ',num2str(Pcu(I)/1000),' kW']);
disp(['Pe = ',num2str(Pe(I)/1000),' kW']);
disp(['Rph = ',num2str(Rph(I)),' ohm']);
disp(['hm = ',num2str(hm),' m']);
disp(['dcu = ',num2str(dcu),' m']);
disp(['lg = ',num2str(lg),' m']);
disp(['yh = ',num2str(yh(I)),' m']);
disp(['Machine mass = ',num2str(Mass(I)),' kg']);
disp(['Voly = ',num2str(Voly(I)),' m^3']);
disp(['Volm = ',num2str(Volm(I)),' m^3']);
disp(['Massm = ',num2str(Massm(I)),' kg']);
disp(['Costm = ',num2str(2*80*12*6),' R']);
disp(['Massy = ',num2str(Massy(I)),' kg']);
disp(['Massw = ',num2str(Massw(I)),' kg']);
disp(['Masstot=',num2str(Masstots(I)),'kg, single stage']);
disp(['Masstot = ',num2str(Masstotd(I)),'kg,2 stages']);
disp(['Axial length = ',num2str(4*hm+2*lg+3*yh(I)),' m']);
disp(['Pcu/Vcu=',num2str(Pcu(I)/(1000*Vcu(I))),' kW/m^3']);
disp(['(Pe+Pcu)/Vcu=',num2str((Pcu(I)+Pe(I))/(1000*Vcu(I))),'kW/m^3']);
disp(['Poutd/Mass=',num2str(Pd/(0.96*1000*Masstotd(I))),' kW/kg']);
disp(['Pout/Mass=',num2str((Pd/2)/(0.96*1000*Masstots(I))),' kW/kg']);
disp(['Efficiency = ',num2str(Eff(I)),' %']);
disp('%****************************************%');
```

Stellenbosch University http://scholar.sun.ac.za

A2 BDC AFPM machine design code listing

```
%******* Design of Axial flux, permanent magnet machine *****
%****** Assuming brushless DC operation ****************
%******* Last updated: 10 November 1999 at 08:00 **********
clear all;
format long;
%*************** Define Constants. ***********************
Rshft = 0.035;                          % Induction machine shaft diameter
yx = 0.0025;                            % Extra yoke added under each magnet
m = 3;                                  % number of phases
kf = 1;                                 % filling factor
q=1;
dcu = 0.008;                            % copper diameter 12 mm
Bg = 0.5;                               % air-gap flux density
n = 2300;                               % speed in rpm
%n = input('Please enter the shaft speed in [rpm]? n = ');
Bgy = 0.4;                              % ratio of Bg/By
hm = 0.005;                             % magnet length of 5 mm
lg = 0.01;                              % airgap length of 14 mm
Ksk = 1;                                % skew factor
%Vd = input('Please enter the desired DC voltage? Vd = ');
Vd = 750;                               % DC Output Voltage of Rectifier
Erms = 0.48*Vd;                         % RMS armature voltage (57.1)
Eph = Erms/0.816;                       % plateau of BLDC phase voltage

%************** Determine J, Nph, dL and ri **************
% ************ constants ********************************
M = 1000;                               % number of data points
mm = 0.001^2;                           % mm^2 meter equivalent
%ro = input('Please enter the outer radius in [m]? ro = ');
ro = 0.34;
dL = linspace(2*lg,ro/2,M);             % delta L
```

Stellenbosch University http://scholar.sun.ac.za

```
ri = ro-dL;                                % inner radius
Kr = ri/ro;                                % ri/ro
g = lg/ro;
re1 = (ro+ri)/2;                           % average radius on magnet [m]
re = sqrt(ro^2+ri.^2)/sqrt(2);             %mass middle point of magnet
Qse = pi*(ri-lg)./(3*re);                  % approximate distribution factor
Ks = 2*sin(Qse/2)./Qse;

%********* Determining the Phase current ****************
%Pd = 322e3;                               %power output 322 kW
Pdev = input('Enter developed power/stage? Pdev = ')*1000;
Iph = Pdev/(Eph);                          % current per stage [A]
Pg1 = 2*Iph*Eph;                           % power at generator terminals [kW]
Ws = 2*pi*n/60;                            % synchronous speed [rad/sec]
T1 = (Pdev/Ws)/2;                          % torque/stage [N.m]

%************ Calculating T, J, Nph ********************
Nph=15*Eph./(pi*n*Bg*dL.*re.*Ks*Ksk);  %serie turns per phase
J=m*Iph*Nph./(kf*dcu*pi*(ri-lg));          % current density [A/m^2]
T=2*pi*kf*(m-1)*J.*Bg*dcu.*(ri-lg).*dL.*re/m;%Torque [N.m]

%********** Calculations of Pmax, Ns ******************
k = (2 + (ri-lg)./re)/3;  % pole arc / pole pitch (11.2)
Pmax = 2*pi*(1-k).*(re)/lg;                % max number of poles
pmx = fix(Pmax);                           % round down all pole numbers
kk = mod(pmx,2);
for i=1:length(Pmax),                      % get rid of odd numbered poles
        if kk(i) == 0,
  P(i) = pmx(i);                           % keep even pole numbers
        else
  P(i) = pmx(i)-1;                         % reduce odd pole numbers by one
        end
end
a = Pmax/2;                                % number of parallel paths
```

Stellenbosch University http://scholar.sun.ac.za

```
f = n*P/120;                                % frequency [Hz]
Ns = ceil(2*a.*Nph./(Pmax*q));% number of turns per coil
Acon = Iph./(a.*J);                         % conductor area
Acus = Ns.*Acon/kf;                         % coil copper area
%Ncp=input('Please enter the number of parallel wires/coil? Ncp = ');
Ncp = 2;
Dwire = sqrt(4*Acon/pi)/sqrt(Ncp);          % conductor diameter [m]

%**Machine losses(Pcu,Pe) and phase resistance (Rph_)******
le = (pi*(ro+ri)./Pmax)+2*lg;               % length of end windings
tc = 75;                                    % conductor temperature
Yt = 0.0039;
P20 = 17e-9;
Pt = P20*(1+Yt*(tc-20));
Rph = 2*m*Nph.^2*Pt.*(dL+le)./(pi*kf*dcu*(ri-lg));% phase resistance (16.2) in
ohm
Pcu = 2*Iph.^2.*Rph;                        % copper losses [Watt]
We = 2*pi*f;
Lwire = Ncp*m*Pmax.*dL.*Ns;                 %active copper length [m]
Pe = pi*Bg^2*We.^2.*(Dwire/2).^4.*Lwire/(8*Pt);% eddy current loss [Watt]
Pg=Pdev-Pcu-Pe;                             % power at terminals [W]
TpJ=T./J;
TpCu = T./Pcu;

%****Volume and mass of yoke, magnets and windings ******
R = 7880;                                   % density of steel kg/m^3
Qp = 2*pi./Pmax;                            % pole pitch in rad
Qm1 = 2*pi*(2+(ri-lg)./(re))./(3*Pmax);     % magnet angle [rad]
Qm = k.*Qp;
Qipg=2*pi*(1-(ri-lg)./re)./(3*P);           %interpolargap angle [rad]
Am = (pi*(ro^2-ri.^2)-2*pi*(1-k).*re.*dL);
Vm = 2*hm*Am;
Volm = 2*(re.*Qm.*dL*hm).*Pmax;             % magnet volume
Volm1 = 4*pi*(re.*dL*hm).*(2+(ri-lg)/ro)/3;
```

Stellenbosch University http://scholar.sun.ac.za

```
yh = 0.5*(re).*Qm*Bgy;                          % yoke thickness [m]
yh1 = pi*Bgy*(3*ro-lg-2*dL)./(3*Pmax );
Voly = pi*(ro^2-ri.^2).*yh;                     % Yoke volume [m^3]
Volw = Acus.*(le+dL).*kf.*q.*Pmax.*m;           % volume of windings
V1 = pi*(ro^2-ri.^2)*lg;                        % volume between ro and ri
V2 = pi*(2*hm+lg)*((ro+2.5*lg)^2-ro^2);         % volume above ro
V3 = pi*(ri.^2-(ri-2.5*lg).^2)*(2*hm+lg);       % volume below ri
Vcu = V1+V2+V3;                                 % volume enclosing the copper
Massy = Voly*R;                                 % mass of yoke in [kg]
Massm = Volm*R;                                 % mass of magnets in [kg]
Massw = R*Volw;                                 % mass of windings
Mmid = R*(re.*Qm.*dL.*yh).*Pmax;                % mass of mid yoke
Masstots=Massm+2*Massy+Massw;%total mass [kg], single stage
Masstotd=2*Massm+2*Massy+2*Massw+Mmid;  %total mass [kg], double stage
Kvcu = (Pcu+Pe)./Vcu;                           % copper loss per copper volume
TpCu=T./Pcu;
PpMass = Pg./Masstots;
Eff = 100*Pg./Pdev;                             % efficiency [%]

clc;
disp('************************************************');
disp('MULTIPLE STAGE AFPM DESIGN OUTPUT RESULTS (Brushless DC
Operation) ');
disp(['.....Date: ',datestr(now),'.....']);
disp('.....');
format short;
[Y,I] = max(TpJ);                               % determine the maximum T/J point
disp(['The optimum design results at ri/ro=',num2str(ri(I)/ro),' are:']);
disp(['Pout = ',num2str(Pg(I)/1000),' kW/stage']);
disp(['T = ',num2str(T(I)),' N.m/stage']);
disp(['Eph = ',num2str(Eph),' V'] );
%disp(['Vd = ',num2str(Vd),' V']);
disp(['Iph = ',num2str(Iph),' A/stage']);
disp(['Pdev = ',num2str(Pdev/1000),' kW/stage']);
```

Stellenbosch University http://scholar.sun.ac.za

```
disp(['n = ',num2str(n),' rpm']);
disp(['ro = ',num2str(ro),' m']);
disp(['dL = ',num2str(dL(I)),' m']);
disp(['ri = ',num2str(ri(I)),' m']);
disp(['Nph = ',num2str(ceil(Nph(I)))]);
disp(['J = ',num2str(J(I)/1e6),' A/mm^2']);
disp(['a = ',num2str(P(I)/2)]);
disp(['lg = ',num2str(1000*lg),' mm']);
disp(['Poles = ',num2str(P(I))]);
disp(['k = ',num2str(k(I))]);
disp(['Pole pitch = ',num2str(Qp(I)),' rad']);
disp(['Magnet angle = ',num2str(Qm(I)),' rad']);
disp(['Interpolar angle = ',num2str(Qipg(I)),' rad']);
disp(['f = ',num2str((P(I)*n/120)),' Hz']);
disp(['Ns = ',num2str(Ns(I)),' turns/coil']);
disp(['Pcu = ',num2str(Pcu(I)/1000),' kW']);
disp(['Pe = ',num2str(Pe(I)/1000),' kW']);
disp(['Rph = ',num2str(Rph(I)),' ohm']);
disp(['yh = ',num2str(yh(I)),' m']);
disp(['Voly = ',num2str(Voly(I)),' m^3']);
disp(['Volm = ',num2str(Volm(I)),' m^3']);
disp(['Volw = ',num2str(Volw(I)),' m^3']);
disp(['Vcu = ',num2str(Vcu(I)),' m^3']);
disp(['Massm = ',num2str(Massm(I)),' kg']);
disp(['Massy = ',num2str(Massy(I)),' kg']);
disp(['Massw = ',num2str(Massw(I)),' kg']);
disp(['Masstot=',num2str(Masstots(I)),'kg, single stage']);
disp(['Masstot=',num2str(Masstotd(I)),'kg, double stage']);
disp(['Axial length = ',num2str(4*hm+2*lg+2*yh(I)),' m']);
disp(['Pcu/Vcu = ',num2str(Kvcu(I)/1000),' kW/m^3']);
disp(['Efficiency = ',num2str(Eff(I)),' %']);
disp('%****************************************%');
```

Stellenbosch University http://scholar.sun.ac.za

B. SINGLE STAGE MACHINE DATA

Table B-1 gives the machine data of the single-stage AFPM machine of Lombard [12].

Table B.1: Prototype AFPM machine data

Inner radius	[mm]	99,6
Outer radius	[mm]	160
Magnet thickness	[mm]	5
Yoke thickness	[mm]	18,2
Air-gap length	[mm]	14
Inter- polar angle	[rad]	0,737
Core flux density	[T]	1,12
Number of turns		132
Air-gap flux density	[T]	0,438
Rated phase current	[A]	32,8
Rated current density	[A/mm]	5,2
Rated torque	[Nm]	29,6
Phase emf @5500rpm	[V]	260
Weight	[kg]	36,2
Copper losses	[W]	200
Cost (active material)	[R]	5464

Stellenbosch University http://scholar.sun.ac.za

C. MEASUREMENTS ON A SINGLE STAGE AFPM MACHINE

This appendix deals with an experimental investigation on the effects of the phase inductance and DC filter inductance on the voltage regulation and power factor of an AFPM machine plus rectifier system. For experimental tests the single stage AFPM machine of Lombard [12] was used (see Appendix B).

The first experimental set-up was without any added series phase inductances or DC filter inductance as shown in Figure C.1. In the second case, inductances were inserted in series with the machine phases in order to increase the machine phase inductance as shown in Figure C.2. In the last case, the rectifier behaviour is investigated with an inductance connected to the DC side of the rectifier as shown in Figure C.3. The series phase inductance of 1,51 mH is about ten times the machine phase inductance. The load consisted of a capacitor bank of 9,2 mF in parallel a resistor bank.

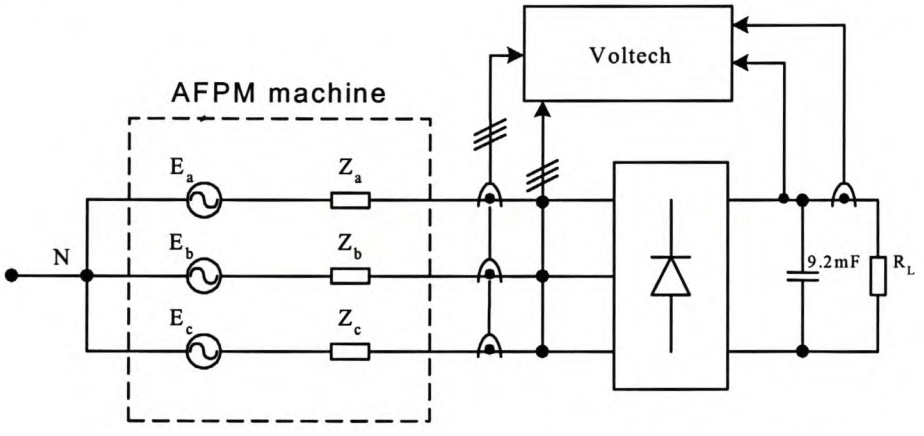

Figure C.1: Experimental set-up with no inductances added.

Stellenbosch University http://scholar.sun.ac.za

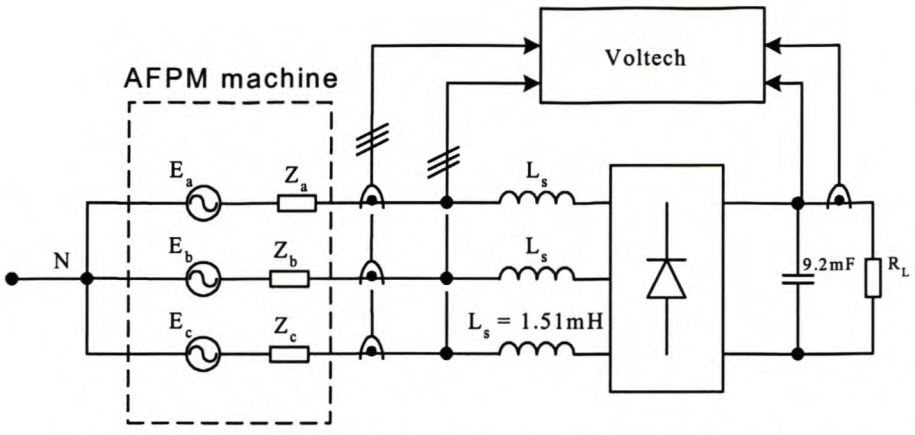

Figure C.2: Series inductances (L_s) added to each phase.

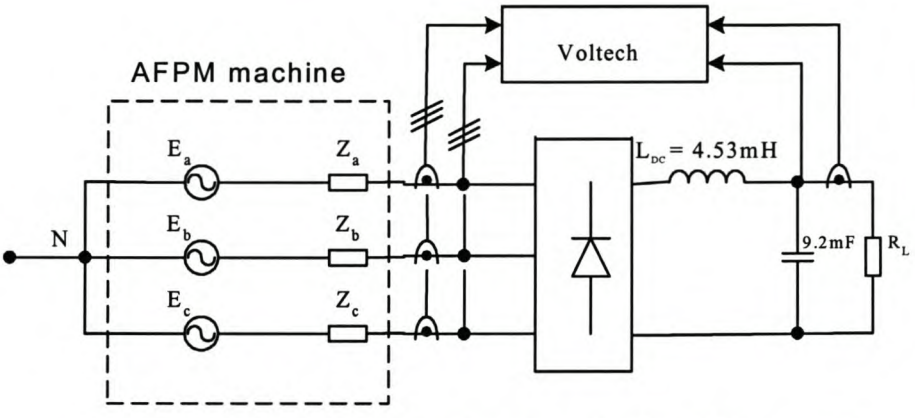

Figure C.3 Inductance added to the DC side of the rectifier.

C.1 Measured results

According to Ray in [18] and Mohan et al. in [9], the maximum regulation in the DC voltage of 3-phase rectifiers from no-load to full-load condition is generally less than 5%. Ray further states that adding a reactance to the DC side of a rectifier gives a better power factor and limits the voltage regulation (VR) from no-load to full-load condition to 4,5%, than adding reactances to the AC side of the circuit. Adding AC reactances was only found beneficial for protection against over-current faults.

In this section the measurements that were taken from the AFPM machine plus rectifier system (Figures C.1 – C.3) are presented. In these measurements the induced EMFs, E_{abc}, of the machine are constant, and not the supply voltages to the rectifier as in [9] and [18]. The DC voltage regulation, thus, will be higher than the figures given

Stellenbosch University http://scholar.sun.ac.za

above. The measurements were taken using a Voltech power analyser. The measured results are given in Table C.1.

Table C.1 Measured results.

Parameter	Case C.1	Case C.2	Case C.3
Inductance	None	1,51 mH	4,53 mH
RMS Line voltage	83,0 V	80,1 V	82,7 V
RMS Phase current	30,9	26,2 A	29,9 A
DC link voltage	104,6V	70,4 V	105 V
DC current	38 A	35 A	38 A
Frequency	88,9 Hz	88,83 Hz	89,02 Hz
Rectifier input power	4127 W	2910 W	4008 W
Rectifier output power	3975 W	2534 W	3990 W
Rectifier efficiency	96 %	87%	99 %
Voltage regulation	6,4 %	9,7 %	6,6 %
Power factor	0,928	0,801	0,947

C.2 Conclusions from measurements

The percentage voltage regulation from no-load to full-load condition obtained from literature [11] on an AFPM generator without rectifier is also in the region of 6 % and, thus, compares well with the results in Table C.1. The voltage regulation is higher than the figures given by [9] and [18] as expected. The voltage drop over the AC reactances inserted in series with the machine phases caused a huge drop in the DC voltage of about 30 %. This also results in a drop in the output power of the same order. It is thus more desirable to put the inductor on the DC side of the rectifier as in Figure C.3, which gives a better efficiency and power factor compared to the other options considered.